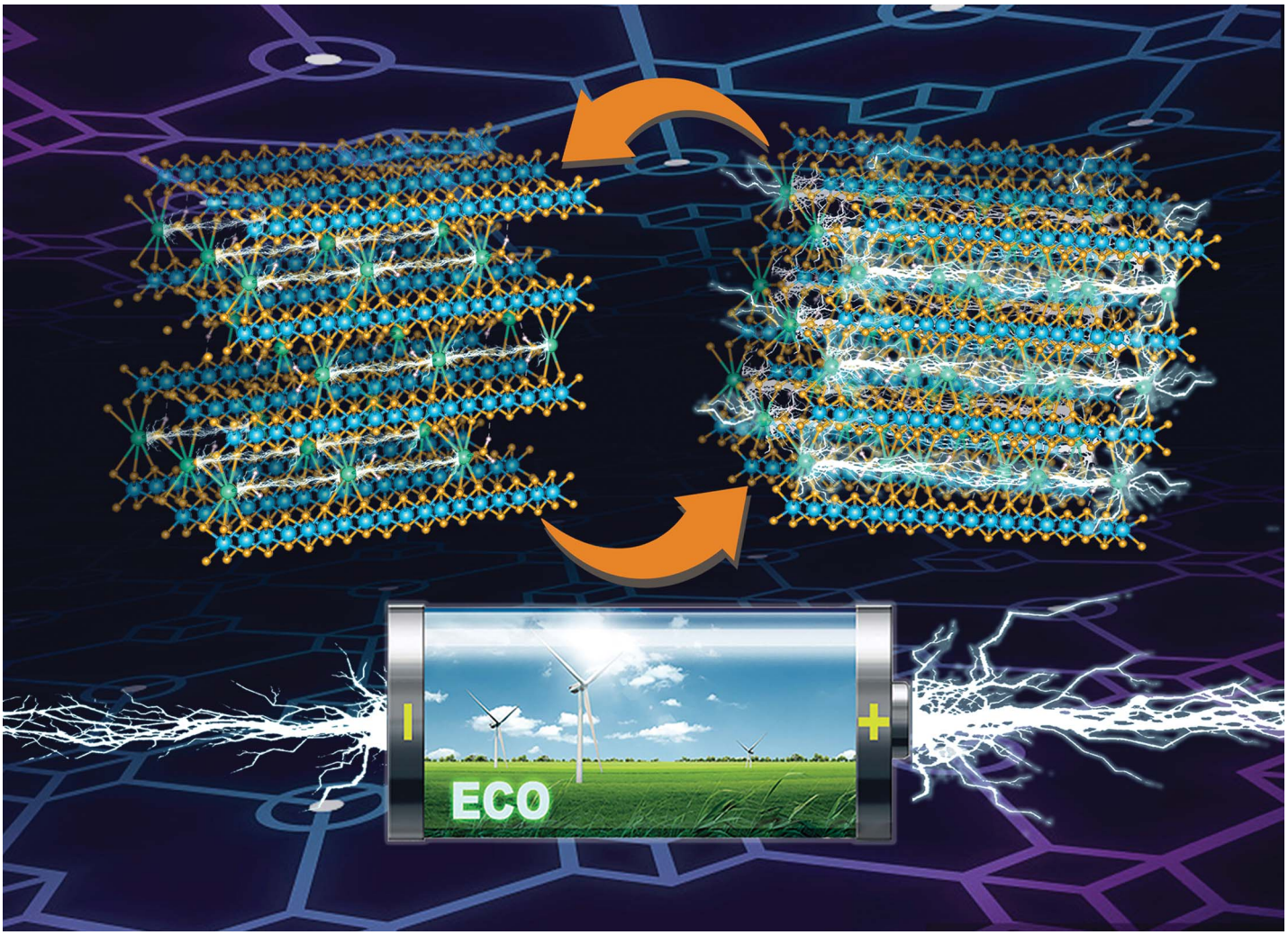

Showcasing research from Professor Yuxin Zhang, State Key Laboratory of Mechanical Transmissions, College of Materials Science and Engineering, Chongqing University, Chongqing, China.

Birnessite based nanostructures for supercapacitors: challenges, strategies and prospects

In this review, the basic properties and preparation strategies of birnessite were summarized and the current challenges were presented. Based on the recent literature and some significant experimental research on birnessite, some new strategies in preparing high electrochemical performance birnessite based nanostructures were highlighted. The present review could help us construct smarter birnessite based structures for supercapacitors.

As featured in:

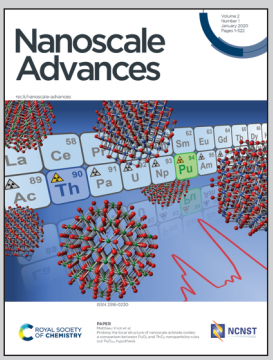

See Yuxin Zhang *et al.*, *Nanoscale Adv.*, 2020, **2**, 37.

ROYAL SOCIETY OF CHEMISTRY

rsc.li/nanoscale-advances

Registered charity number: 207890

Nanoscale Advances

REVIEW

Cite this: *Nanoscale Adv.*, 2020, **2**, 37

Birnessite based nanostructures for supercapacitors: challenges, strategies and prospects

Shijin Zhu, †[ab] Wangchen Huo,†[a] Xiaoying Liu [c] and Yuxin Zhang *[a]

Received 31st August 2019
Accepted 21st September 2019

DOI: 10.1039/c9na00547a

rsc.li/nanoscale-advances

In the past few years, intensive attention has been focused on birnessite based electrodes for supercapacitors. Much progress has been achieved in developing birnessite based nanostructures with high electrochemical performance. However, challenges still remain in taking full advantage of birnessite and building smart structures to overcome the gap between the obtained capacitance and its theoretical capacitance. In this review, the basic information on birnessite and its preparation strategies are summarized and the current challenges are put forward. Finally, some new strategies for preparing high electrochemical performance birnessite based nanostructures are highlighted.

1. Introduction

Birnessite, also called δ-MnO_2, an oxide mineral of manganese along with calcium, potassium and sodium, has always been deemed to be a promising material in many application areas because of its unique layer structure resulting in a high specific surface area and abound chemically active sites.[1–3] It is well accepted that birnessite is not a typical manganese oxide, but a hydrous manganese oxide (HMO), formed by edge-sharing MnO_6 octahedra with various combinations of cationic species and H_2O molecules according to the particular birnessite species.[4,5] Additionally, the valence of Mn in birnessite is not onefold, but combines Mn^{2+}, Mn^{3+} and Mn^{4+} in the bulk phase corresponding to the charge quantity of combined cations, which maintains the charge stability of the crystal structure.[6,7] Thus, birnessite is a kind of semi-stable crystal. Not only the layer spacing, but also the species of intercalated cations and the amount of interlayer water of birnessite can be altered.[5,8–10] Hence, some physical and chemical properties of birnessite can be adjusted based on its multifarious constituents, forms, configurations, *etc.*, which find applications in many areas such as oxidation, catalysis, battery technology, water splitting, waste treatment, *etc.*

In recent years, birnessites have been widely used as active materials for electrochemical capacitors (ECs).[11–17] The

[a]State Key Laboratory of Mechanical Transmissions, College of Materials Science and Engineering, Chongqing University, Chongqing, 400044, P. R. China. E-mail: zhangyuxin@cqu.edu.cn

[b]Institut für Chemie, Technische Universität Chemnitz, Straße der Nationen 62, 09111 Chemnitz, Germany

[c]Engineering Research Center for Waste Oil Recovery Technology and Equipment, Ministry of Education, College of Environment and Resources, Chongqing Technology and Business University, Chongqing 400067, China

† These authors contributed equally to this work.

Shijin Zhu received his M.S. degrees in Materials Science and Engineering from Chongqing University (CQU) in 2015 (Prof. Yu Xin Zhang's group). Currently, he is a PhD. candidate in the Department of Polymer Chemistry at Chemnitz University of Technology (TUC), Germany, under the supervision of Prof. Michael Sommer. His research interests involve polymer based porous carbon and self-assembled nanostructures for energy storage materials.

Wangchen Huo received his bachelor's degree in Material Shaping and Control Engineering in 2015 from Jingchu University of Technology. Now, he is a doctoral candidate in Chongqing University. His research interests are related to the design and application of nanomaterial for photocatalysis and supercapacitors.

theoretical capacitance of Mn-based oxides can be calculated based on the average charge transfer energy of Mn^{4+} to Mn^{3+} and Mn^{3+} to Mn^{2+}.[18–20] Similar to other Mn-based oxides, the theoretical capacitance of birnessite is also close to 1370 F g^{-1}, but it is reduced by the inherent low valence Mn in the bulk of birnessite. However, these inherent low valence Mn are always coupled with some intercalated cations (Na^+, K^+, Ca^{2+}, *etc.*), which can be consumed and released during the charging–discharging process and then generate capacitance or capacity.[11,21] Additionally, the electrochemical properties of the birnessite electrode are not only influenced by its morphology, structural size, specific surface area (SSA), *etc.* which can be handled easily, but also affected by some inherent factors like electronic conductivity, ionic conductivity, adsorption activity, *etc.* Thus, researchers are mainly focusing on the following three main points: (1) designing and fabricating nano-size birnessite for enhancing the specific surface area and electrochemically active sites.[22–25] (2) Altering the morphology and construction of birnessite for improving contact with the electrolyte.[26,27] (3) Reducing the dead mass of birnessite to increase the active material's utilization.[28–30] Based on these strategies, birnessites are always designed as ultrathin films and grow on the surface of some conductive substrates as these ultrathin films are not self-sustaining. Thus, a series of birnessite based nanostructures were designed, including novel pure birnessite,[31–33] birnessite/carbon nanocomposites,[34–37] birnessite/metal oxides nanocomposites,[38–42] birnessite/polymer nanocomposites,[43–46] *etc.* and some of these structures exhibited ideal electrochemical properties. However, for most birnessite based electrodes, the capacitances still range from 15–25% of its theoretical capacitance. Thus, attention should not be entirely focused on these macroscopical methods and some new strategies should be put forward.

More recently, in order to improve the electrochemical performances of birnessite based electrodes, scientists have gradually shifted their interests to the intrinsic structure of birnessite, for example, enhancing the electronic conductivity of birnessite itself by doping other element atoms (*e.g.* Co, Ni, Cu, *etc.*) into the crystal structure, adjusting the ionic conductivity by increasing the interlayer spacing and improving their electrochemical activity by manufacturing defects in their crystal lattices.[47,48] In these well-designed strategies, some of the properties like capacitance were improved, while rate capability or cycling stability was reduced and *vice versa*. Thus, some research studies took a different tack by increasing or reducing the content of one or two components.[49–51] And the applied working potential windows can be enlarged to even over 1.23 V in an aqueous electrolyte, which exceeds expectation. By rationally designing and matching the positive electrode and negative electrode the working potential window of an assembled device can be increased to 2.6 V in 1.0 M Na_2SO_4 with almost three times the energy density obtained. However, the capacitance values are still the weakness. Actually, for almost all of the birnessite based structures, the capacitance values are still lower than 400 F g^{-1}, about 30% of the theoretical capacitance of Mn-based oxides.[52–61] As one of the most easily adjustable Mn-based oxides, there are still lots of strategies and possibilities to improve its electrochemical performances.

In this review, we intend to provide a comprehensive overview of birnessite based nanostructures through in-depth discussion of the overall crystalline information, energy storage mechanism, morphology and structure, electrochemical performance, and practical applications. Furthermore, the performance bottlenecks of birnessite based electrodes are put forward and the corresponding solutions are proposed.

2. Crystal information of birnessite

As one member of the phyllomanganate family, birnessite possesses a two-dimensional layered structure, composed of alternating stacked Mn–O layers (edge-shared MnO_6 octahedra) and hydration alkali cations (Na^+, K^+, *etc.* restricted in the interlayer region).[8,62] Like α-MnO_2, β-MnO_2, λ-MnO_2 and γ-MnO_2, the basic unit of birnessite is also MnO_6 octahedra with one Mn atom surrounded by six O atoms closely and uniformly (Fig. 1a). For a single MnO_6 octahedron layer (Fig. 1b), every Mn

Dr Xiaoying Liu received her bachelor's degree in Inorganic Nonmetallic Materials from Hebei University of Engineering in 2007. She received her M. Eng. and PhD. degrees in Materials Science and Engineering from the Chongqing University in 2011 and 2018, respectively. Now Dr. Liu is a full lecturer in the College of Environment and Resources in Chongqing Technology and Business University. Dr Liu's research interest is the preparation of nanomaterials for energy storage devices and photocatalysis.

Dr Yu Xin Zhang received his B. Eng. and M. Eng. in Chemical Engineering from Tianjin University in 2000 and 2003, respectively. He received his PhD. degree in Chemical and Biomolecular Engineering from the National University of Singapore (NUS) in 2008, and continued to work as a research fellow in Prof. Hua Chun Zeng's group at NUS until 2009. Now Dr Zhang is a full professor in the College of Materials Science and Engineering in Chongqing University. Dr Zhang's research interest is self-assembled nanostructures for energy storage materials and photocatalysts.

atom is also surrounded by six O atoms along the *c* axis, which means that the Mn atoms are distributed in the layer uniformly. However, the surrounding six atoms do not lie in the same plane when observed along the *α* axis (Fig. 1c), with three of them lying on the top of Mn atoms and the other three under the Mn atoms. Additionally, several hydration alkali cationic species, like H^+, Na^+, K^+, Ca^{2+}, *etc.* are locked in the interlayer. Thus, the crystal structure of birnessite is confirmed (Fig. 1d). The interlayer spacing of birnessite is usually ~7 Å.[8,62,63] Due to the replaceability of hydration alkali cations in the interlayer region, the spacing could be increased to ~10 Å upon further hydration to form a layered structure with double the crystal water, which closely-related birnessite is buserite structure,[64] whilst the spacing can be decreased to ~5.5–5.6 Å by dehydration. In addition, owing to the presence of cations in the interlayer region, the oxidation state of manganese is not totally tetravalent, and the average states commonly fall between 3.6 and 3.8, suggesting the presence of mainly Mn(IV) with little Mn(III) in the birnessite structure.[8,49,62]

Because of the layer structure feature, the XRD patterns (*e.g.* JCPDS: 80-1098; 86-0666) often exhibit diffraction peaks at around 12° and 25° corresponding to the interlayer spacing and half interlayer spacing (001 and 002 planes).[65,66] Another two diffraction peaks often appear at around 36° and 66°, matching the 111 and 020 planes (Fig. 2a). These diffraction intensities depend on the crystalline degree and grain size. However, these diffraction peaks do not always belong to the 001, 002, 111 and 020 planes because of the existence of many subtype birnessites due to the different interlayer cationic species and variation of the interlayer (JCPDS: 86-0666; 18-0802; 23-1046; 27-0751; *etc.*). Because of the faster crystalline growth along the *a* and *b* axis compared to the *c* axis, the morphology of reported birnessite is often nanofilms or nanosheets, with an interlayer spacing of 0.24 nm and ~0.7 nm corresponding to the distance between adjacent Mn atoms and interlayer spacing (Fig. 2b–d).[67,68]

3. Energy storage mechanism of birnessite

The energy storage mechanism of birnessite based electrodes can be classified as a MnO_2 electrode with both electrical

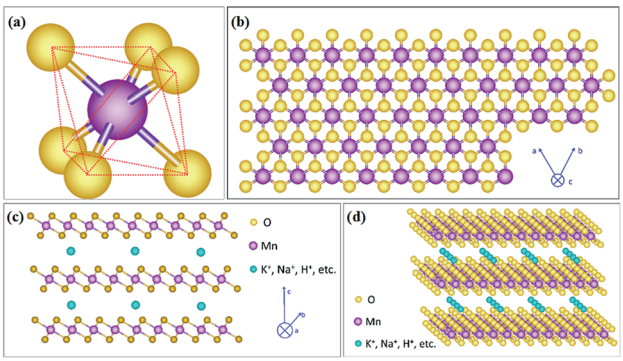

Fig. 1 (a) MnO_6 octahedron unit; (b) schematic diagram of birnessite along the 001 plane; (c) schematic diagram of birnessite viewed along the 011 plane; (d) stereoscopic schematic diagram of birnessite.

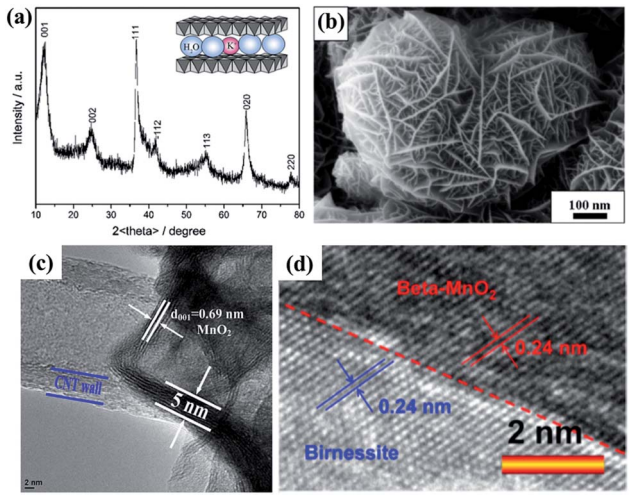

Fig. 2 (a) Typical XRD pattern of birnessite.[65] (b) SEM image of typical birnessite.[67] (c) and (d) HRTEM images of typical birnessite.[49,68]

double-layer capacitance (EDLC) and faradaic pseudocapacitance involved.[18,69–72] Specifically, the EDLC is a kind of surface adsorption–desorption behavior existing in almost all of the electrodes. Similar to a parallel-plate capacitor, charge separation happens with a tight charge layer forming on the surface of birnessite based electrodes after being inserted into the electrolyte and an appropriate voltage was applied between these two electrodes.[73–76] The EDLC can be estimated by referring to the following equation:

$$C = A\varepsilon_r\varepsilon_0/d$$

where *A* is the specific surface area of the electrode accessible to the electrolyte ions, ε_r is the electrolyte dielectric constant, ε_0 is the permittivity of a vacuum, and *d* is the effective thickness of the EDL (the Debye length). Based on the equation above, the capacitance is directly proportional to the specific surface area of the applied active materials. Thus, a high SSA is always expected during the fabrication process of birnessite.

Another energy storage mechanism of birnessite based electrodes is pseudocapacitance coming from the valence state changes.[77,78] During the charge–discharge process, the alkaline cations (Na^+, K^+, H^+, *etc.*) in the electrolyte can be absorbed by the O atoms of the MnO_6 octahedron because of the opposite electrical properties between alkaline cations and O atoms and then charges were transformed to the adjacent Mn atom whose valence changes from +4 to +3 as follows:

$$(MnO_2)_{surface} + C^+ + e^- \rightarrow (MnO_2{}^-C^+)_{surface}$$

where C^+ = Na^+, K^+, Li^+, *etc.* Note that this charge storage mechanism only involves the surface atoms of the birnessite crystallites or a very thin layer and it is an ultrafast process which cannot be differentiated from EDLC clearly. Nevertheless, this process is very similar to the surface adsorption–desorption mechanism but it is an electrochemical reaction process, which enhances the capacitance to a great extent.[79,80] Thus, the

thickness of the 'thin layer' is the key point for enhancing the capacitance of birnessite electrodes.

Apart from the above two mechanism, the energy storage mechanism of birnessite electrodes also contains an intercalation–deintercalation process.[81,82] In this process, protons (H^+) or alkali metal cations (C^+) such as Li^+ intercalate into the bulk of the material upon reduction followed by deintercalation from the bulk of the material upon oxidation as follows:

$$MnO_2 + C^+ + e^- \rightarrow MnOOC$$

where $C^+ = H^+$, Na^+, K^+, Li^+, *etc.* Two ion-intercalating models are concurrent in birnessite electrodes separated by the ion transfer route. Specifically, one is the electrolyte ions getting across the crystal lattices of birnessite, and the other is the electrolyte ions moving through the gap (tunnel or interlayer space) of the crystal lattices, as the interlayer spacing (001 plane) of birnessite is large enough (0.72 nm) and this spacing can be adjusted by the size of the intercalated cations. Additionally, these intercalated cations can be released during the charge process and consumed during the discharge process, and this contributes capacitance or capacity to the birnessite based electrode.[83,84] However, this process is more like a battery reaction process rather than a capacitive reaction process as this is a kind of chemical reaction rather than charge transfer, which can be separated from the first two energy storage mechanisms by defining as diffusion-controlled contribution and surface capacitive contribution by analyzing the CV data at various sweep rates according to a power law equation as follows:

$$i = av^b$$

where i is the current (A), v is the sweep rate (V s^{-1}), a and b are adjustable parameters fluctuating with the voltage. The b-values reflecting the electrode performance were calculated from the slope of the plot of log i *vs.* log v. A well-defined condition, $b = 1.0$, is representative of a capacitive response because the current is proportional to the sweep rate. The measured current from the surface capacitive contribution follows a linear law approximately because of the ultrafast reaction process, which is different from the diffusion-controlled contribution.[85–87] A quantitative distinction of different capacitive contributions to the overall charge storage was provided based on the following equation:

$$i(V) = k_1 v + k_2 v^{1/2}$$

For analytical purposes, this equation was divided with the square root of the scan rate, then:

$$i(V)/v^{1/2} = k_1 v^{1/2} + k_2$$

where $k_1 v$ and $k_2 v^{1/2}$ correspond to the current contributions from the surface capacitive effects and the diffusion-controlled intercalation process, respectively, i(V) is the current at a given voltage, v is the scan rate and k_1 and k_2 are constants fluctuating with the scan rate calculated from plotting the sweep rate dependence of the current at each fixed potential (k_1: the slope of a straight line; k_2: the y-axis intercept point of a straight line).[88]

In recent publications, high intercalated cation content birnessites were synthesized by adjusting the species of intercalated cations or oxidizing Mn_3O_4 crystals *via* an electrochemical oxidation method. Meanwhile, the energy mechanism of Mn based oxides with pre-inserted cations (alpha-MnO_2 and birnessite) was revised as follows:[89]

Charge process:

$$M_xMnO_2 \rightarrow MnO_2 + xM + xe^- \ (M^+ = H^+, Na^+, K^+)$$

Discharge process:

$$MnO_2 + xM + xe^- \rightarrow M_xMnO_2 \ (M^+ = H^+, Na^+, K^+)$$

However, in this revised mechanism, the pseudocapacitance was misunderstood because the source of the pseudocapacitance was ignored. Actually, the energy storage process of birnessite based electrodes includes two steps. In the first step, once the birnessite based electrode, being a positive electrode, was immersed in the electrolyte together with a negative electrode, charge separation happens and an electric double layer forms. Meanwhile, the alkaline cations (Na^+, K^+, H^+, *etc.*) in the electrolyte are absorbed by the O atoms of the MnO_6 octahedron because of the opposite electrical properties between alkaline cations and O atoms and then charges were transferred to the adjacent Mn atom whose valence changes from +4 to +3. In the second step, these absorbed alkaline cations are released along with these pre-inserted cations during the charge process and consumed during the discharge process. Thus, not all the participating alkaline cations come from the pre-insertion process or component cations. Additionally, the energy storage process involved in the revised mechanism mainly comes from diffusion-controlled contribution rather than surface capacitive contribution. However, the capacitance of these prepared structures is enhanced a lot and the potential window was found to be increased to 1.2 V or even 1.3 V in an aqueous electrolyte because the potential window for K^+ extracted is around 1.2 V. Based on these results, some high voltage asymmetrical supercapacitors (2.7–2.8 V) were assembled, which possess very high energy density.[50,51]

4. Challenges for birnessite based electrodes

In fact, at the present stage, the research hotspot is still the electronic conductivity of birnessite which influences the subsequent electrode reaction by gathering charges originating from electrochemical reactions. These gathered charges not only increase the operating potential windows within a short time resulting in an incomplete electrochemical reaction between birnessite and the electrolyte leading to a low

capacitance, but also block the secondary response of active materials to the electrolyte generating a low rate capability. Introducing a conductive matrix into the birnessite based electrode is always a popular approach, but no great breakthroughs have been achieved yet. Note that the intrinsic conductivity of birnessite seems to be the key point, which determines the upper limit of birnessite based electrodes. Thus, charge transfer in the interior of birnessite should be taken into consideration.

Another challenge is the balance of the crystalline degree of birnessite and its specific surface area. Many research studies have reported that it is very hard to achieve these two factors simultaneously, as a high crystalline degree means few defects in birnessite crystals, which means a low specific surface area. However, a higher crystalline degree will provide higher intrinsic conductivity for birnessite, which is very important for the electrode, while enhancing specific surface area is considered to be the most effective strategy to obtain high capacitance. Thus, some new projects aimed at enhancing the crystalline degree of birnessite and its specific surface area simultaneously should be proposed.

Finally, the component of birnessite should be taken into account. The theoretical capacitance of MnO_2 is as high as 1370 F g^{-1}. For some narrow tunnel MnO_2 structures, like beta-MnO_2, lambda-MnO_2 and gamma-MnO_2, the low obtained capacitance can be ascribed to the ultrahigh dead mass in the electrode as there is no room to store electrolyte ions in their bulk. However, for birnessite, most obtained capacitances still range from 200–400 F g^{-1}, which is far below its theoretical capacitance. As we know, the theoretical capacitance of MnO_2 is calculated based on the valence transition of Mn^{3+} to Mn^{4+}, which happens in the whole operating potential window, while the capacitance of MnO_2 is determined by the content of Mn^{4+}, which will influence the adsorption capacity of electrolyte ions. Nevertheless, the content of Mn^{3+} in birnessite is around 33%. Although some results have demonstrated that the intrinsic electronic conductivity of birnessite can be enhanced by increasing the content of Mn^{3+}, balancing the content of Mn^{3+} and the adsorbing capacity of birnessite is necessary.

5. Strategy of enhancing electrochemical properties

5.1 Enhancing conductivity

The electronic conductivity of active materials is often supposed to be one of the main factors affecting their electrochemical properties as charges originating from electrochemical reactions have to be transferred to an external circuit quickly, or these superfluous charges will impede further electrochemical reactions. The strategies for enhancing the electronic conductivity are often divided into two categories: one is introducing conductive materials to increase the total specific conductance of birnessite based structures; the other is improving the intrinsic conductivity of birnessite to overcome the weakness of electric conductivity.

5.1.1 Birnessite/conductive species composite. Carbon based nanomaterials possess lots of advanced properties, including high specific surface area, abound electrochemically active sites, light weight and high electronic conductivity, and were deemed as the most perfect supplementary materials for birnessite based electrode structures.[73,90] Three main kinds of carbon materials, including graphene,[91–95] carbon nanotubes[96–101] and porous carbon,[102–104] are widely investigated in view of their good electrical conductivity and excellent mechanical/electrochemical stability.

Graphene, as a two-dimensional, one atom thick and highly flexible carbon, has been widely used in electrodes, not only as an energy storage material but as a conductive supporting material, because of its high electrical conductivity (10^4 S cm^{-1}), ultrahigh theoretical specific area (2630 m^2 g^{-1}) and excellent electrochemical stability.[105] The high surface area and conductive graphene has the ability to accelerate the charge transfer and promote the reaction kinetics indeed during charge storage. Peng *et al.*[106] have demonstrated that the energy storage process of the birnessite/graphene composite with a layer by layer structure should occur at the layer spaces and it is very hard or impossible for charges or ions to cross the graphene layer (Fig. 3a). The uniform distribution (Fig. 3b) and high crystalline degree birnessite (Fig. 3c) guarantees the layer-by-layer structure with high flexibility and high controllability. A planar supercapacitor (Fig. 3d) prepared by an etching method along the desired trajectory exhibits excellent rate capability with only 22% capacitance loss when the current density increases by a factor of 20 (from 0.5 to 10 A g^{-1}) (Fig. 3e). Thus, a high energy density (18.64 W h kg^{-1}) with a maximum power density of 12.6 kW kg^{-1} was obtained for this planar supercapacitor (Fig. 3f). As a flexible supercapacitor, the flexibility was tested in three physical states (flat, folded and rolled), and a very similar capacitance was obtained for these three states (Fig. 3g). Additionally, over 90% of the capacitance was retained for the device after being folded thousands of times (Fig. 3h). These results highlighted the high electronic conductivity and flexibility of graphene which can be inherited by birnessite/graphene composites to generate special electrodes.

Compared to graphene, carbon nanotubes (CNTs) are a 1D highly crystalline tubular carbon with a diameter of several tens of nanometers, which possess very high electronic conductivity, high mechanical strength and high chemical stability providing an effective charge transfer route. Additionally, the surface properties of multiwalled carbon nanotubes can be changed by various methods without decreasing their electronic conductivity markedly, which ensures more approaches to fabricate birnessite/CNT composites. Wu and co-authors[107] reported self-standing and highly flexible δ-MnO_2@CNTs/CNT composite films using a three step strategy (Fig. 4a). The CNTs were prepared through a CVD process and used as the substrate to load birnessite with the surface of these CNTs changing from smooth to rough (Fig. 4b and c). The self-standing flexible films were obtained by a vacuum filtration method with CNTs and birnessite/CNT composites applied alternately (Fig. 4d). Thus, these free-standing electrodes are supposed to have excellent

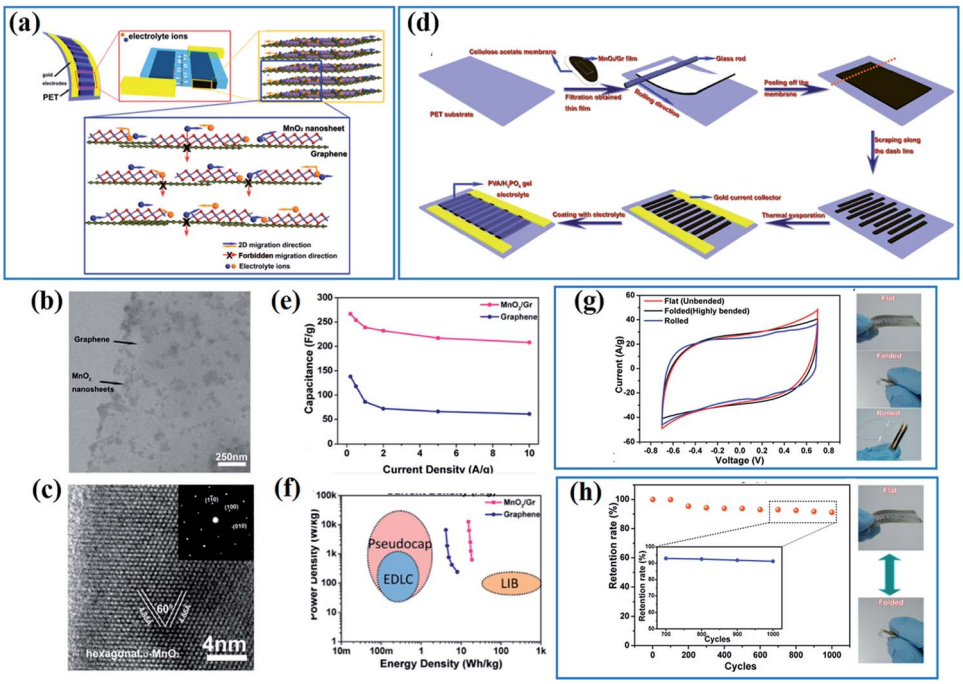

Fig. 3 (a) Design of hybrid 2D birnessite/graphene structure based planar supercapacitors; (b and c) TEM images of the 2D hybrid structure with birnessite nanosheets integrated on graphene surfaces; (d) schematic of fabrication procedures for ultraflexible planar supercapacitors; (e) comparison of specific capacitance values for the hybrid supercapacitors and those based on graphene. (f) A typical Ragone plot of the as-fabricated supercapacitors. (g) CV curves of the planar supercapacitor under three different bending states and demonstration of three different bending states: flat, folded, and rolled; (h) cycling stability under repeated flat/folded cycles and demonstration of the flat/folded cycle when testing cycling stability.[106]

electrochemical properties. There is only about 15% fading of the capacitance when the discharge current increased from 0.2 A g^{-1} to 5 A g^{-1} (Fig. 4e). Additionally, the specific capacitance remains almost unchanged with the mass of the electrode increasing from 1.97 to 6.18 mg cm^{-2} and the area capacitance increasing linearly, indicating the high porosity and high conductivity of these self-standing film electrodes (Fig. 4f and g), while both the specific capacitance and volumetric capacitance remain unchanged with the diameter of the electrode increasing. Moreover, the specific capacitance was slightly reduced with the bending angle applied from 0 to 180° (Fig. 4h). These results highlighted the outstanding mechanical properties and excellent electrochemical performance, as well as easy processing of birnessite/CNT free standing electrodes.

Besides conductive carbon species, highly conductive metals are also a favorable additive used for supporting birnessite. These conductive metals should possess high chemical inertness which ensures a stable and highly conductive substrate. Among all the conductive metals, Au is the most attractive material due to its high electronic conductivity and high ductility, which may not only provide the electrode with high electrochemical performance but some special physical properties as well. Qiu *et al.*[108] reported a template method using PS spheres as a sacrificial template to fabricate a Au@birnessite nanomesh (Fig. 5a(i)). Au was used not only as a substrate to support birnessite but also as a conductive path for charges (Fig. 5a(ii)). Additionally, the uniform pores originating from the sacrificial PS spheres facilitate ion transfer (Fig. 5a(iii and iv)). Thus, excellent rate capabilities were obtained for this structure (Fig. 5a(v)). When connecting two devices together, a perfect superimposed charge–discharge curve was obtained (Fig. 5a(vi)). The excellent electrochemical properties are surely ascribed to the high electronic conductivity of Au, which was inherited by the Au@birnessite nanomesh. Zhu and co-authors[109] coupled mesoporous gold with birnessite, which ensures a high electronic conductivity and fast ion transition (Fig. 5b(i–iii)). These mesoporous gold@birnessite nanostructures can be pressed into an electrode directly without any extra current collectors due to the high ductility of Au (Fig. 5b(iv)). The electrode exhibited a high capacitance of 906.4 F g^{-1} and good rate capability because of the high conductivity originating from mesoporous gold (Fig. 5b(v and vi)).

Although the electronic conductivity of birnessite based composites can be improved by introducing exterior conductive species and the rate capacitance was enhanced obviously, the capacitance still lies in a low level if high mass loading birnessite was applied. Note that the conductivity of materials always followed a "short slab" principle for a single conducting path. Thus, the intrinsic conductivity of birnessite should not be ignored.

5.1.2 Enhancing intrinsic conductivity. The intrinsic conductivity of birnessite is lower than that of most Mn-based crystals, like alpha-MnO_2, beta-MnO_2, lambda-MnO_2, *etc.* because of its unique layer structures and relatively poor

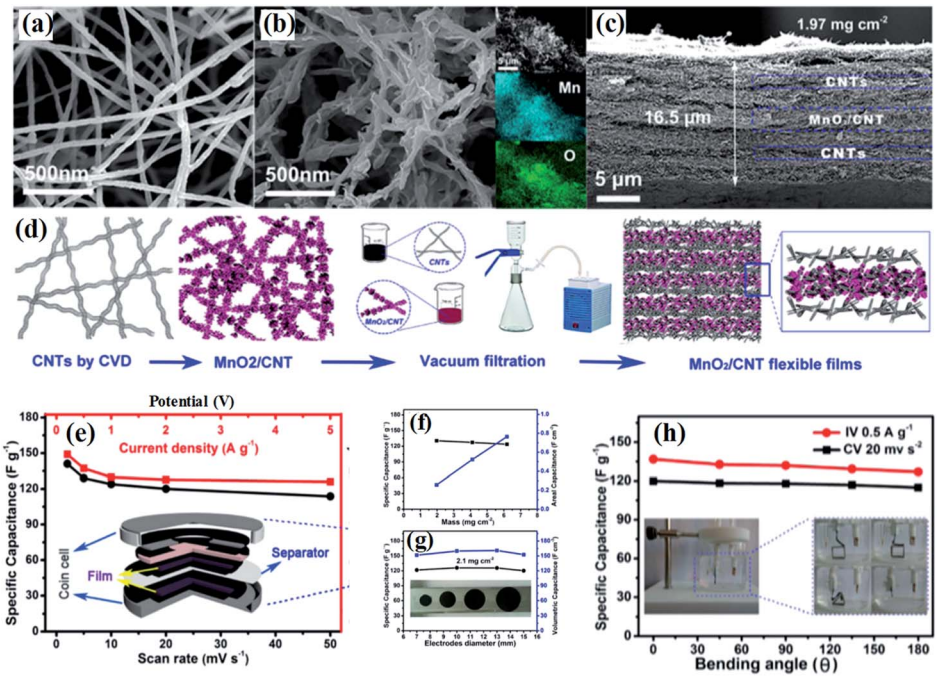

Fig. 4 (a and b) SEM images of raw CNTs; SEM images of birnessite@CNT composites, insets show the EDS elemental mapping images, showing the spatial distribution of Mn and O; (c) cross section of a unit of the birnessite@CNTs/CNT stacked film with a thickness of 16.5 μm; (d) schematic of the preparation process of stacked films; (e) dependence of specific capacitance on the scan rate (bottom axis) and on the current density (top axis) determined from the CV curves and GCD curves, respectively; (f) mass (left axis) and areal (right axis) specific capacitance as a function of the areal mass of the flexible films calculated from the GCD curve; (g) dependence of mass (left axis) and volumetric specific capacitance (right axis) on the diameter determined from the discharge curves at 0.5 A g^{-1}. A photograph of the flexible electrodes with different diameters (inset); (h) specific capacitance change with bending angles calculated from the CV curves (black) and GCD curves (red). The inset shows photographs of the three-electrode configuration.[107]

crystalline degree. Previous research has shown that there is no single valence state of Mn in birnessite, but a combination of +2, +3 and +4.[2,4] These polytropic valences of Mn provide an alternative specific conductance as a "double-exchange" mechanism happens in Mn(III)–O–Mn(IV) structures, triggering novel electron transport behavior.[110] Specifically, the electrical

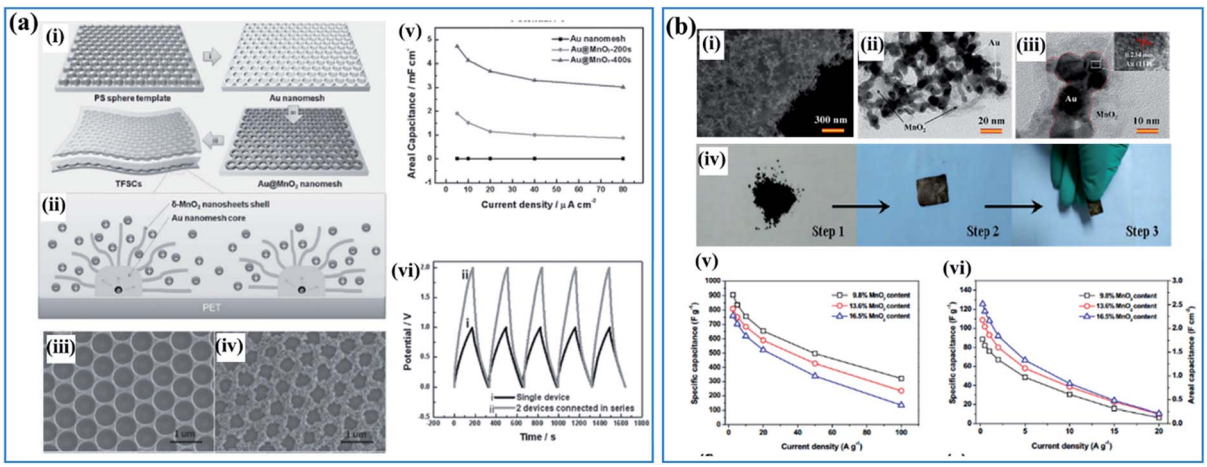

Fig. 5 (a) Au@birnessite core–shell nanomesh: (i) schematic illustration of the fabrication of the Au@birnessite nanomesh-based TFSC; (ii) schematic diagram of ion diffusion pathways and charge transport channels of the Au@birnessite nanomesh electrode; (iii) SEM image of the Au nanomesh; (iv) SEM image of the Au@birnessite core–shell nanomesh peeled from the PET substrate; (v) the areal capacitance of the Au nanomesh, Au@birnessite–200s and Au@birnessite–400s as a function of the current density; (vi) the galvanostatic charge/discharge curves of a single device and 2 devices connected in series at 5 μA cm^{-2}.[108] (b) Mesoporous gold networks@birnessite: (i) FIB/SEM image of the Au@birnessite network (16.5 wt% birnessite); (ii, iii) TEM images of the Au@birnessite network (16.5 wt% birnessite); (iv) the preparation process of the electrode; (v) specific capacitances of Au@birnessite networks at different current densities based on the weight of birnessite; (vi) specific capacitances of the Au@ birnessite network at different current densities based on the whole weight of the electrode.[109]

conductivity of manganese oxide with mixed valence states (Mn^{3+} and Mn^{4+}) is higher than that with a single valence state (Mn^{3+} or Mn^{4+}).[111] Mn^{3+} ions possess 4 electrons in the d orbital and they can split into 3 local electrons with lower energy (itinerant electron) in the t_{2g} orbital and an itinerant electron with higher energy in the e_g orbital in the MnO_6 crystal field. Thus, the electronic structure of the Mn^{3+} ion is altered into $t_{2g}^3e_g^1$. The higher energy electron in the e_g orbital can jump from Mn^{3+} to Mn^{4+} according to double-exchange interactions through the O^{2-} ion, since the e_g orbital in the Mn^{4+} ion is empty. Then, the Mn^{4+} ion can transform into a Mn^{3+} ion, and the adjacent electron in the e_g orbital of Mn^{3+} ion can jump into the 2p orbital of O^{2-} forming a Mn^{3+}–O–Mn^{4+} route. Thus, the electrical conductivity of mixed valence state manganese oxide is enhanced by jumping of the itinerant electron and the electrical conductivity is influenced by the ratio of Mn^{3+}/Mn^{4+} (Fig. 6a(i and ii)).

Based on the "double-exchange" mechanism, the intrinsic resistance of birnessite was reduced by increasing the content of Mn^{3+} within limits, which will influence its electrochemical properties markedly. Zhu *et al.*[49] reported structural directed growth of ultrathin parallel birnessite on β-MnO_2 with birnessite standing on the surface of β-MnO_2 parallelly (Fig. 6b(i)) and a high Mn^{3+} content. The crystal structure of the as-prepared birnessite changed slightly because of the restriction of the crystal lattice of beta-MnO_2, which enhanced the electrochemical properties (Fig. 6b(ii–iv)). Birnessite displayed a regular box-like shape and an ultrahigh capacitance of 657 F g^{-1} based on the weight of parallel birnessite and 306 F g^{-1} based on the whole weight of the nanocomposite in 1 M Na_2SO_4 electrolyte (Fig. 6b(v)). Additionally, excellent rate capability was found as the conductivity of this nanostructure improved a lot, which can be ascribed to the increased content of Mn^{3+}. Thus, approximately 74% of the capacitance was retained when the current density increased from 0.25 A g^{-1} to 64.0 A g^{-1} (Fig. 6b(vi)). A device assembled with the as-prepared nanostructure as the positive electrode and reduced graphene oxide as the negative electrode gives a high energy density of 40.4 W h kg^{-1} at a power density of 275 W kg^{-1} as the potential window of the device was increased to 2.2 V (Fig. 6b(vii)).

Although the electronic conductivity was improved because of the increased content of Mn^{3+} and the dead mass of birnessite was reduced because of the unique structure and ultrathin birnessite films, the dead mass of the whole structure increased as beta-MnO_2 was introduced, which contributed little to the capacitance, resulting in a very high capacitance based on the weight of birnessite but ordinary capacitance based on the weight of the whole mass of the structure. However, a new idea of enhancing the electrochemical properties of birnessite was put forward and can be optimized further.

5.1.3 Metal doping. The intrinsic conductivity of birnessite can also be modulated by the metal doping method without interface restriction as the crystal structure or physical interaction of birnessite can be adjusted by doping with Au, Ag, Ce, V, Al, Cu, Mg, Co, *etc.*[112–119] Additionally, these doped heteroatoms can function as the electron donor to regulate the electron structure of MnO_2, which is responsible for a better capacitive performance. Liu *et al.* reported a V-doped birnessite structure by the reduction of potassium permanganate with concentrated hydrochloric acid. The morphology of the as-prepared V-doped birnessites changed a little and the AOS of Mn decreased a little with increasing content of vanadium atoms. The capacitance of these structures increases with increasing content of vanadium atoms and then goes down,

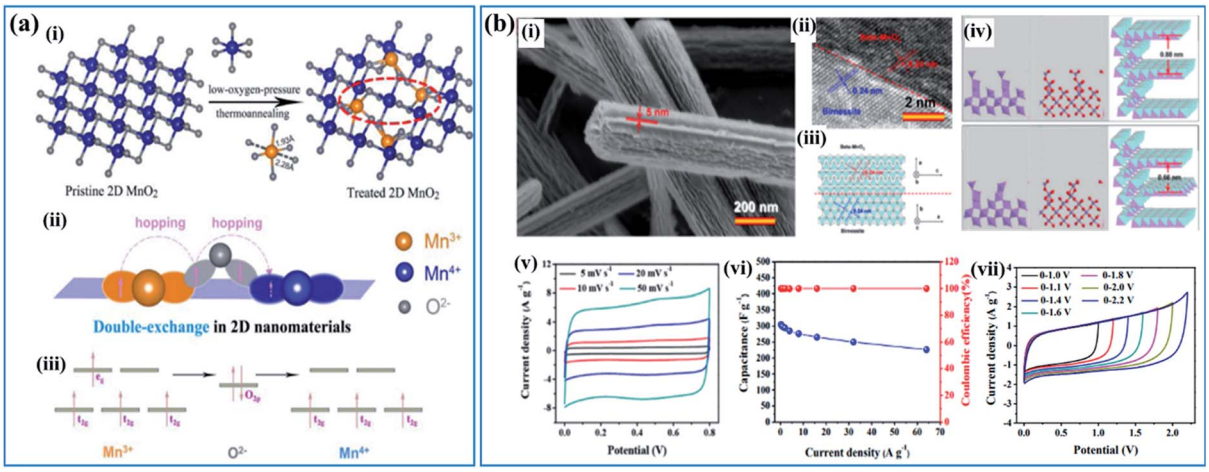

Fig. 6 (a) Double-exchange mechanism in birnessite: (i) diagram of low-oxygen-pressure thermo-annealing treatment to achieve double-exchange of Mn(III)–O–Mn(IV) in the treated birnessite nanosheet. (ii, iii) Double-exchange of Mn(III)–O–Mn(IV) results in magnetoresistance in the 2D birnessite nanosheets.[110] (b) β-MnO_2/parallel birnessite core/shell nanorod: (i) SEM image of β-MnO_2/parallel birnessite core/shell nanorods; (ii) high resolution TEM image of a β-MnO_2/parallel birnessite core/shell nanorod; (iii) structural representation of a β-MnO_2/parallel birnessite core/shell nanorod (perpendicular to the 001 plane of parallel birnessite); (iv) structural computation of a β-MnO_2/parallel birnessite core/shell nanorod (formation 1 and formation 2); (v) cyclic voltammograms at different scan rates (potential window: 0–0.8 V); (vi) variations of the capacitance and coulombic efficiency with the current densities (potential window: 0–0.8 V); (vii) CV curves of β-MnO_2/parallel birnessite//AGO ASC at different cell voltages at a scan rate of 50 mV s^{-1}.[49]

which can be ascribed to the increased electronic conductivity. The sample named HB-V 15% exhibited the highest capacitance of 241 F g^{-1} and retained about 246 F g^{-1} after 200 cycles.[48] Peng *et al.* reported a Mo-doped hexagonal birnessite by a solvothermal method and used it as a supercapacitor electrode. The crystalline degree of the as-prepared birnessite and its morphology become worse and worse with increasing content of doped heteroatoms (Mo) which may be ascribed to the destroyed crystal structure because of the high content of the doped heteroatom (Mo) resulting in a poor conductivity. Thus, these nanostructures have pretty poor electrochemical performance.[115]

A detailed investigation of Fe-doped birnessite including crystallinity, morphology, valence states, crystal structure, electronic structure, conductivity and electrochemical performance was proposed by Tian's group.[114] Specifically, the crystalline degree of Fe-doped birnessite become poorer and poorer (Fig. 7a) and the average particle sizes become smaller and smaller (Fig. 7b) with the increase of the amount of the Fe dopant. These can be ascribed to the formation of defects (*e.g.* vacancies) and distortions, which can hinder crystal growth in the host structure after Fe doping. Moreover, the relative percentage of Mn(III) decreases progressively as the content of the Fe dopant increased (Fig. 7c), confirming that Mn(III) was substituted by Fe(III) in the doped birnessite samples. The electron charge density of Fe-doped birnessite exhibits an enlarged Fe–O bond (2.086 Å) compared with the Mn–O bond (2.060 Å) because of the ionic character of Fe atoms (Fig. 7d), resulting in a metabolic electronic structure of birnessite. Thus, the band gap of birnessite can be reduced after Fe doping as revealed by DFT calculations, leading to the increase of the intrinsic electronic conductivity of doped-birnessite (Fig. 7e). Hence, an enhanced rate capability related to the electronic conductivity of birnessite was found (Fig. 7f).

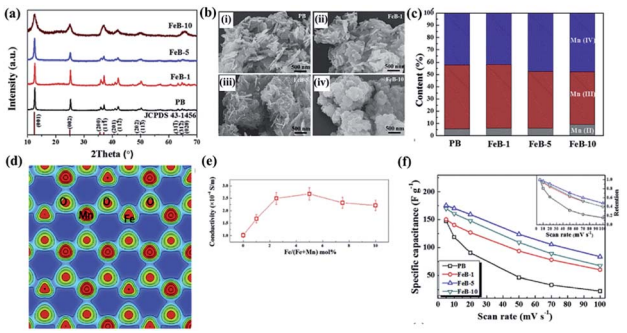

Fig. 7 (a) XRD patterns of PB, FeB-1, FeB-5, and FeB-10 samples; (b) SEM images taken from PB, FeB-1, FeB-5, and FeB-10 samples; (c) the relative content of Mn(II), Mn(III) and Mn(IV) in these prepared samples calculated from the corresponding XPS spectral fitting; (d) electron charge density distribution of Fe-doped birnessite with 33.3 mol% Fe content viewed along the (001) plane; (e) electrical conductivities of the prepared birnessite samples changing with the molar percentage of Fe; (f) comparison of the specific capacitances of PB, FeB-1, FeB-5 and FeB-10 samples at different scan rates. The inset shows capacitance retention of these samples at different scan rates.[114]

These results demonstrate the ion transport kinetics, electron structure and crystal structure can be altered by doping with heteroatoms to some extent. However, the variation of these properties is not always benin. Suitable heteroatoms should be selected by first-principles calculations as some heteroatoms may destroy the original electronic conductive path. Additionally, metal doped birnessite may have optimized conductivity and reaction kinetics resulting in enhanced electrochemical properties, which calls for atomic-scale and highly dispersive doping. Some *in situ* studies on the intrinsic reaction process and the interaction mechanism between the doped atoms and MnO_2 also provide a lot of inspiration to construct high-performance electrodes.

5.2 Crystal dimensional regulation

Despite the high specific surface area and abundant electrochemically active sites, the electrical conductivity of birnessite is pretty low, compared to other crystal type Mn-based oxides, because of the high content of crystal water, sparse atoms and poor crystalline degree, resulting in a large amount of dead mass in birnessite based electrodes which cannot be used for energy storage. Thus, reducing the dead mass in birnessite based electrodes is always the greatest demand for enhancing the energy density of supercapacitors. Many strategies have been developed to reduce the crystalline size to reduce the dead mass or increase the utilization ratio of birnessite, thus providing some superiority for supercapacitor application.

5.2.1 Ultrathin birnessite films. For birnessite based electrodes, electrochemical reactions occur not only on the surface according to the EDLC mechanism and pseudocapacitance mechanism, but also in the interlayer based on the alkaline intercalation–deintercalation mechanism. The thickness of the birnessite films determines the numbers of Mn–O layers, resulting in the amount of electrochemical active sites decreasing with increasing thickness of the birnessite films. Thus, reducing the thickness of birnessite films is the most direct and most efficient way to reduce their dead mass and then enhance their electrochemical performance. Zhao *et al.*[120] reported a hydrothermal method to synthesize hierarchical birnessite nanoflowers composed of thin birnessite films. These hierarchical birnessite nanoflowers exhibit a high specific capacitance of 197.3 F g^{-1} with good cycling stability. About 94.6% of the initial capacitance was retained after 1000 cycles. However, although the surfaces of the flowers are very porous, the composed birnessite films are very thin and easy to be involved in the electrochemical reaction and the interior of birnessite flowers is very dense and not accessible to electrolyte ions, which means that the content of dead mass in these birnessite flowers is still very high. In the past few years, lots of reported birnessite based electrodes exhibited the same disadvantage, displaying a capacitance range from 100–200 F g^{-1}.[65,121–124]

5.2.2 Hollow structure. In recent years, some studies have been aimed at reducing the thickness of birnessite films as well as cutting down the unnecessary dead volume by designing some hollow structures, including tube-like structures, sphere-

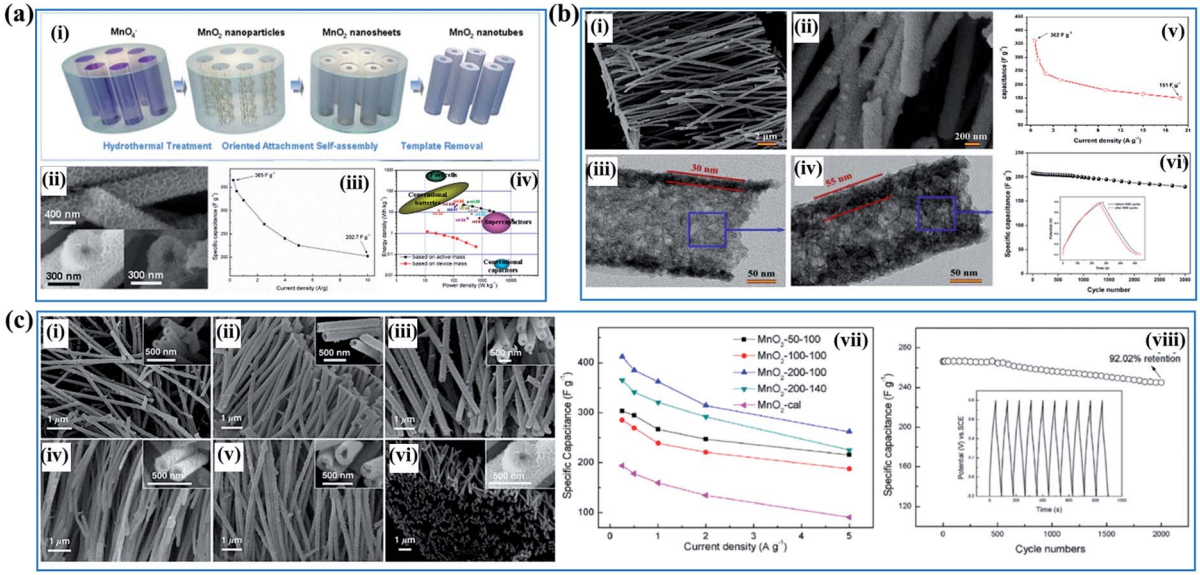

Fig. 8 (a) Porous birnessite nanotubes: (i) schematic illustration of the procedure to synthesize porous birnessite nanotubes; (ii) SEM images of birnessite nanotubes; (iii) specific capacitance of birnessite nanotubes measured under different current densities; (iv) (e) the energy density *vs.* power density of the birnessite nanotubes//AG asymmetric supercapacitor.[33] (b) Coaxial double nanotubes: (i, ii) SEM and TEM images of coaxial double nanotubes with inner birnessite and outer amorphous carbon; (iii and iv) SEM and TEM images of coaxial double nanotubes with outer birnessite and inner amorphous carbon; (v) specific capacitance of coaxial double nanotubes with outer birnessite and inner amorphous carbon measured under different current densities; (vi) variations of capacitance with cycle numbers for coaxial double nanotubes with outer birnessite and inner amorphous carbon with insets showing the comparison of galvanostatic charge–discharge curves before and after 3000 cycles.[125] (c) Porous birnessite tubular arrays: SEM images of birnessite nanotubes: (i) birnessite-50–100, (ii) birnessite-100–100, (iii) birnessite-200–100, (iv) birnessite-50–140, (v) birnessite-100–140, and (vi) birnessite-200–140; (vii) specific capacitance under different current densities; (viii) cycling performance of birnessite-200–100 at a current density of 5 A g^{-1}. The inset shows the charge–discharge curves of the last 10 cycles of the MnO_2-200–100 electrode.[126]

like structures and specific template-like structures. Huang *et al.*[33] fabricated a tube-like structure assembled from ultrathin birnessite nanofilms *via* a hard template method (Fig. 8a(i and ii)). These nanotubes exhibited excellent electrochemical properties, including high specific capacitance (365 F g^{-1}), good cycling stability (90.4% retained after 3000 cycles) and high energy density (22.5 W h kg^{-1}) obtained from a MnO_2 nanosheet-built nanotubes//AG asymmetric supercapacitor as this structure consisted of ultrathin birnessite films and the dead mass in this structure is reduced to a very low content (Fig. 8-a(iii, iv)). Moreover, the tube-like structure provides an extra contact area for the electrolyte which enhanced the utilization ratio of active materials greatly. However, the large thickness of the tube wall is still a big problem for enhancing the electrochemical properties, which will decrease the ion transfer significantly. Thus, Zhu *et al.*[125] reported a birnessite tube assembled with ultrafine birnessite chippings by a spontaneous reaction between amorphous carbon and $KMnO_4$ (Fig. 8b(i, ii)). The thickness of the tube wall can even be adjusted to 30 nm (Fig. 8b(iii, iv)), while the crystalline degree of the birnessite structure cannot be well controlled because of the mild reaction conditions. The specific capacitance obtained for this structure is close to that in previous work (362 F g^{-1}), while the rate capability and cycling stability of the structure were enhanced a lot as the thickness of the tube wall was controlled, which improves the ion transfer (Fig. 8b(v, vi)). Based on these studies, Li *et al.*[126] carried out a detailed study by adjusting the thickness of the tube wall and the diameter of the tube (Fig. 8c(i–vi)), and the specific capacitance of the structure was optimized to 411.9 F g^{-1} and the rate capability and cycling stability were enhanced a lot (Fig. 8c(vii and viii)). Besides, the electrochemical properties of the tube-like birnessite structure are also influenced by the length of the tube, crystalline degree and arrangement of the films. By rational combination of these factors, all properties of the tube-like birnessite structure can be improved on a large scale.[127]

For sphere-like hollow structures and specific template-like structures, the main preponderance is that the morphologies of these structures are easy to be controlled and can be scaled up as templates are often applied in these strategies.[128–131] These structures often possess high specific capacitance and good rate capability as the hollow structure can be used as a transit depot for the electrolyte, which shortens the ion transfer distance. Zhang *et al.* reported a yolk and hollow structure assembled with ultrathin birnessite films which gives a high specific capacitance of 273 F g^{-1} with good rate capability. In this structure, colloid carbon spheres were used as the sacrificial template which can be adjusted by controlling the pH values of the reaction solution.[132] Munaiah *et al.* prepared hollow birnessite spheres assembled from ultrathin birnessite films with a very poor crystalline degree by a soft template method. The hollow sphere displayed a capacitance of 283 F g^{-1} in 0.1 M

$Ca(NO_3)_2$ solution. However, the cycling stability of this structure is very poor with 37% of its initial capacitance being lost after 1000 cycles, which may be because the hollow sphere was crushed during the charge–discharge process.[133] In recent years, some studies reported using biological materials as the template to support ultrathin birnessite for supercapacitors as some biological materials possess unique pores which are considered to be one of the most important factors affecting their electrochemical properties. Zhang's group reported many studies on ultrathin birnessite films and diatomite which exhibited outstanding electrochemical properties including high specific capacitance and excellent rate capability.[38,134–136] However, most of the studies did not give very good cycling stability, which can be ascribed to the crushing of active materials during the testing process.

Although the specific capacitance of birnessite has been improved a lot by these strategies, the electronic conductivity of the obtained birnessite structure had not been enhanced resulting in poor rate capability. Additionally, the dimensionality of these structures is designed to be smaller and smaller leading to poor mechanical strength, which influences the cycling stability to a great extent.

5.2.3 Lightweight material replacement. Although ultrathin birnessite films possess favorable electrochemical performance, their physical and chemical stability still needs to be enhanced urgently. For ultrathin birnessite films or single layer birnessite films, it is very hard to maintain their initial state after drying. One strategy based on coupling birnessite with some lightweight materials was proposed. These lightweight materials may not possess any special properties, but they replace the dead mass of birnessite and significantly reduce the applied mass of active materials and enhance its electrochemical properties.[38,137–140] Very recently, Liu and co-authors[104] reported a block polymer derived a uniform mesoporous carbon supported birnessite composite which enables ultrafast electron and ion transport (Fig. 9a). The as-prepared fibers are very porous even after coupling with birnessite (Fig. 9b–d). A textile cloth of porous carbon fiber@birnessite exhibits outstanding electrochemical performance (Fig. 9e). A high *b*-value close to 1.0 indicates the excellent capacitive properties of these structures (Fig. 9f). An ultrahigh ratio of fast-kinetics process even at a very low scan rate implies an ultrahigh utilization and very low dead mass of birnessite (Fig. 9g and h). Thus, both gravimetric capacitance and areal capacitance were boosted (Fig. 9i). Undeniably, the high conductivity of porous carbon plays a very important role in its electrochemical performance. The ultrahigh capacitance is mainly contributed by the reduced dead mass. These results indicate that the utilization of birnessite can be enhanced and dead mass can be reduced dramatically by replacing the dead volume of birnessite with lightweight materials.

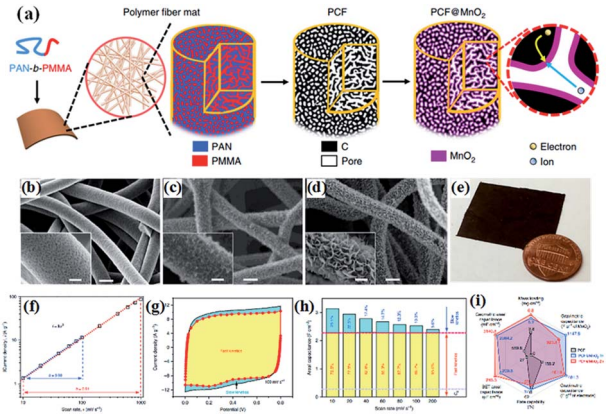

Fig. 9 (a) Schematic illustration of the synthesis of PCF and PCF@birnessite; SEM images of (b) PCF, (c) PCF@birnessite-1h, and (d) PCF@birnessite-2h; (e) a photograph of a piece of the PCF@birnessite-2h electrode next to a U.S. penny with a diameter of ~1.9 cm; (f) absolute current density and scan rate follow the power law, $i = kv^b$, in both the slow and fast scan rate regions; (g) decoupling of the capacitance contributed by the fast-kinetic processes (yellow) and the slow-kinetic processes (blue); (h) histograms of the capacitance contributions by the different processes: yellow, fast-kinetic processes; blue, slow-kinetic processes; C_{dl}, electrical double layer capacitance; (i) the radar chart compares six figures-of-merit of PCF (black), PCF@birnessite-1h (blue), and PCF@birnessite-2h (red): mass loading of the active materials, rate capability (from 10 to 1000 mV s^{-1}), gravimetric capacitance based on the mass of birnessite and active materials, and areal capacitance based on the geometric area and BET surface area. All capacitances are obtained at 10 mV s^{-1}.[104]

5.3 Defect engineering

Recent studies have shown that the conductivity and charge storage can be effectively improved by introducing anion or cation vacancies into birnessite because of the promoted surface redox reaction kinetics resulting in an enhanced electrochemical performance.[141–143] Especially, for birnessite with oxygen vacancies, the oxygen vacancies would lead to charge compensation by changing the oxidation states of Mn ions (Mn^{2+}, Mn^{3+}, and Mn^{4+}) in birnessite, which will further result in variation of the charge carrier density and make the deficient birnessite more conductive.[144] Additionally, oxygen vacancies are capable of providing additional ion intercalation sites to effectively improve the specific capacitance of birnessite. Gao *et al.*[145] reported birnessite with Mn vacancies with a controllable amount of vacancies by reassembling the as-exfoliated birnessite at different pH values. The flocculated nanosheet samples exhibit 3D porous nanostructures and equilibration at different pH values has no influence on their morphologies (Fig. 10a–c). XANES spectra of protonated birnessite exhibit a higher intensity of P', where the weak pre-edge peaks P and P' correspond to the dipole-forbidden 1s–3d transition, indicating the coexistence of Mn^{3+} and Mn^{4+} (Fig. 10d). Moreover, a negative shift of the main absorption peaks with the decrease of pH values was found after taking the derivative of XANES spectra, indicating that lower pH progressively reduces Mn to the trivalent state (Fig. 10e). Additionally, high-energy X-ray scattering and pair distribution function analysis were performed to characterize the content of Mn vacancies. Two main pair distribution function peaks, the in-plane Mn–Mn peak at 2.89 Å and the Mn–Mn_{surf} distance at 3.45 Å, related to the content of Mn vacancies were considered (Fig. 10e). The content was

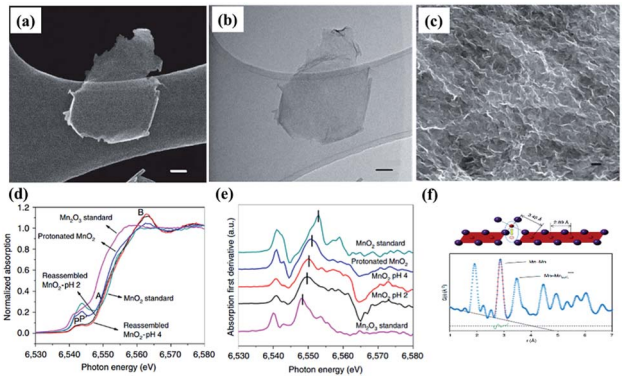

Fig. 10 (a) SEM image and (b) bright-field TEM image of exfoliated birnessites, scale bar, 50 nm; (c) SEM image of reassembled birnessite nanostructures treated in pH = 2 solution for 24 h, scale bar: 500 nm; (d) XANES spectra of protonated birnessite, pH = 2 and 4 treated reassembled birnessite; (e) first derivative curves corresponding to the samples; (f) models of in-plane Mn–Mn and Mn surface and pair distribution function analysis of reassembled birnessite.[145]

calculated to be 18.3% at pH <1, 26.5% at pH = 2 and 19.9% at pH = 4 because of Jahn–Teller distortion, and may be accommodated in crystalline birnessites (Fig. 10f). Based on these results, the as-prepared Mn vacancy birnessite delivered a greatly enhanced capacitance value of over 300 F g^{-1} (1 M Na_2SO_4 electrolyte) and improved cycling performance.

5.4 Synergistic effect

In recent years, many articles have demonstrated that the electrochemical properties of birnessite can be enhanced by introducing another one or two components into birnessite based materials and the electrochemical performance of the introduced components can also been improved, which can be ascribed to the changing of the charge transfer route, interaction of the same involved ions or heterojunction enhanced electrical performances.[16,146–153] In well-designed materials, the dead mass of birnessite was decreased because the utilization of birnessite was enhanced, resulting in improved capacitance, rate capability and cycling stability. Zhu *et al.* reported CeO_2@birnessite core–shell heterostructures using both CeO_2 octahedra and nanowires as the cores to support birnessite (Fig. 11a(i–vi)). These CeO_2 nanowire@birnessite nanostructures exhibited unprecedented pseudocapacitance performance (255 F g^{-1}) with outstanding rate capability and high energy density (Fig. 11a(vii and viii)). A new mechanism for the enhanced rate capability has been proposed. Specifically, during the electrochemical test, the CeO_2 cores act as an accelerator. In the process of oxidation, CeO_2 and birnessite release their electron at the same time due to the mandatory potential difference. However, the high activity of CeO_2 makes it easy to be oxidized and reduced during the oxidation–reduction process. Thus, CeO_2 depopulates the electrons from MnO_2 uninterruptedly which enhances the degree of oxidation of birnessite resulting in an enhanced electrochemical performance and *vice versa*. However, such approaches often suffer from poor electronic conductivity of these inorganic

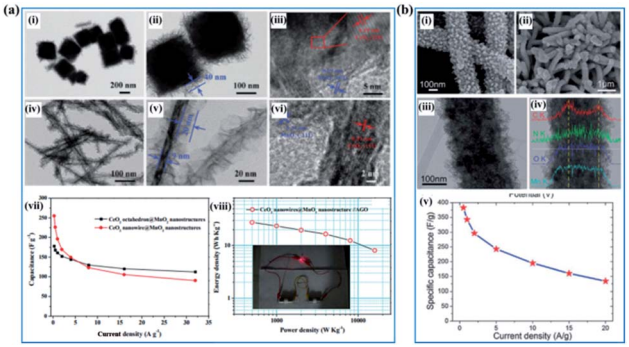

Fig. 11 (a) CeO_2@birnessite core–shell heterostructures: (i–iii) TEM images of the CeO_2 octahedron@birnessite nanostructure; (iv–vi) TEM images of the CeO_2 nanowire@birnessite nanostructure; (vii) specific capacitance under different current densities; (viii) Ragone plots of the CeO_2 nanowire@birnessite nanostructure//active graphene oxide (AGO) asymmetric supercapacitor. The inset shows the digital image of a red light-emitting diode (LED) lit by the as-prepared device.[154] (b) PANI–birnessite coaxial nanofibers: (i, ii) SEM image of PANI nanofibers; (ii) low- and high-magnification SEM images; (iii) TEM images (inset shows the SAED pattern); (iv) line-scanning (indicated by a white line) of the PANI–birnessite coaxial nanofibers; (v) the specific capacitance as a function of different current densities.[46]

nanomaterials.[154] Jiang and co-authors[46] reported the synergistic effect of birnessite and polyaniline with K-birnessite grown on the surface of polyaniline (Fig. 11b(i–iv)). The as-prepared PANI–birnessite coaxial nanofibers with optimal composition, when applied as an electrode, exhibited a high specific capacitance (383 F g^{-1} at 0.5 A g^{-1}) with a good rate in 1 M Na_2SO_4 aqueous solution, which is attributed to the synergistic effects of the combined pseudo-capacitive contributions from the core and shell (Fig. 11b(v)).

There are also lots of papers reporting the "synergistic effect" of birnessite and other metal oxides,[39,41,68,155–157] metal hydroxides,[158–161] metal sulfides,[162,163] or layered double hydroxides (LDHs),[87,164–166] which enhanced the electrochemical properties by reducing the dead mass of birnessite. Liu *et al.* reported Co_3O_4 nanowire@MnO_2 (birnessite) ultrathin nanosheet core/shell arrays by a three-step hydrothermal method (Fig. 12a). These nanocomposites exhibit not only high specific capacitance (480 F g^{-1}), but also high areal capacitance (0.56 F cm^{-2}). Additionally, the cycling stability was also improved (97.3% retention after 5000 cycles). The combination of MnO_2 and

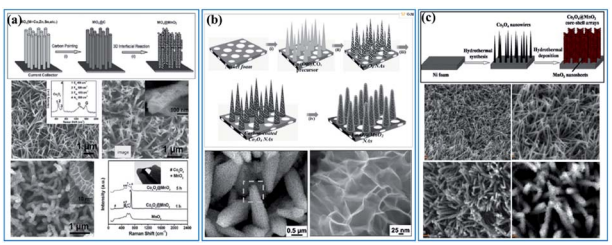

Fig. 12 (a) Co_3O_4 nanowire@birnessite ultrathin nanosheet core/shell arrays.[155] (b) Co_3O_4@birnessite hierarchical nanoneedle arrays.[167] (c) Hierarchical Co_3O_4@birnessite core–shell arrays.[68]

Table 1 The uniqueness and difference of these strategies for adjusting the electrochemical performance of birnessite based electrodes

Strategy	Active materials	Capacitance	Rate capability	Cycling stability	Electrolyte	Ref.
Enhancing conductivity	2D birnessite/graphene hybrid nanostructures	267 F g^{-1} at 0.2 A g^{-1}	78 (0.2 to 10 A g^{-1})	92% (after 7000 cycles)	PVA/H_3PO_4	106
	Birnessite@CNTs/CNTs composite	149 F g^{-1} at 0.2 A g^{-1}	85% (0.2 to 5 A g^{-1})	90% (after 5000 cycles)	1 M Na_2SO_4	107
	Au@birnessite core–shell nanomesh	4.72 mF cm^{-2} at 5 μA cm^{-2}	63.7% (5 to 80 μA cm^{-2})	95% (after 1000 cycles)	1 M Na_2SO_4	108
	Mesoporous gold networks@birnessite	906.4 F g^{-1} at 2.5 A g^{-1}	72.2% (2.5 to 20 A g^{-1})	97.2% (after 5000 cycles)	1 M Na_2SO_4	109
	Parallel birnessite/β-MnO_2	306 F g^{-1} at 0.25 A g^{-1}	74 (0.25 to 64 A g^{-1})	92% (after 3000 cycles)	1 M Na_2SO_4	49
	Vanadium doped birnessite	246 F g^{-1} at 0.2 A g^{-1}	85 (0.2 to 1.6 A g^{-1})	NA	1 M Na_2SO_4	48
	Fe doped birnessite	175.6 F g^{-1} at 5 mV s^{-1}	NA	110 F g^{-1} (after 6000 cycles)	1 M Na_2SO_4	114
	Molybdenum-doped birnessite microspheres	202 F g^{-1} at 0.1 A g^{-1}	65.3 (0.1 to 2 A g^{-1})	90% (after 2000 cycles)	1 M Na_2SO_4	115
Crystal dimensional regulation	Birnessite nanoflowers	197.3 F g^{-1} at 1.0 A g^{-1}	64.3% (1.0 to 10 A g^{-1})	94.6% (after 1000 cycles)	1 M Na_2SO_4	120
	Mesoporous birnessite nanotubes	365 F g^{-1} at 0.25 A g^{-1}	55% (0.25 to 10 A g^{-1})	90.4% (after 3000 cycles)	1 M Na_2SO_4	168
	Coaxial mesoporous birnessite/aCNT nanotubes	362 F g^{-1} at 0.5 A g^{-1}	41.7 (1.0 to 20 A g^{-1})	88.6% (after 3000 cycles)	1 M Na_2SO_4	125
	Birnessite hollow sphere	188 F g^{-1} at 0.5 mA cm^{-2}	52% (0.5 to 10 mA cm^{-2})	63% (after 1000 cycles)	0.1 M $Ca(NO_3)_2$	133
	PCF@birnessite	481.3 F g^{-1} at 10 mV s^{-1}	57% (10 to 200 mV s^{-1})	98% (after 5000 cycles)	6 M KOH	104
Defect engineering	3D porous birnessite nanosheet	306 F g^{-1} at 0.2 A g^{-1}	~40% (0.2 to 10 A g^{-1})	92% (after 1000 cycles)	1 M Na_2SO_4	145
	Mixed-valence birnessite	2530 F g^{-1} at 0.61 A g^{-1}	96 (0.61 to 122.7 A g^{-1})	NA	1 M Na_2SO_4	142
Synergistic effect	CeO_2@birnessite core–shell heterostructures	255 F g^{-1} at 0.25 A g^{-1}	62.9 (0.25 to 32 A g^{-1})	90.1% (after 3000 cycles)	1 M Na_2SO_4	154
	Polyaniline–birnessite coaxial nanofiber	383 F g^{-1} at 0.5 A g^{-1}	35 (0.5 to 20 A g^{-1})	75.5% (after 2000 cycles)	1 M Na_2SO_4	46
	Co_3O_4 nanowire@birnessite nanosheet arrays	480 F g^{-1} at 2.67 A g^{-1}	56 (4 to 44.7 mA cm^{-2})	97.3% (after 5000 cycles)	1.0 M LiOH	155
	Co_3O_4@birnessite hierarchical nanoneedle arrays	1905.4 F g^{-1} at 0.5 A g^{-1}	43.2 (0.5 to 10 A g^{-1})	89.8% (after 5000 cycles)	1.0 M LiOH	167
	Hierarchical Co_3O_4@birnessite core–shell arrays	560 F g^{-1} at 0.2 A g^{-1}	54.5 (0.2 to 10 A g^{-1})	95% (after 5000 cycles)	1.0 M LiOH	68

Co_3O_4 with a unique morphology and independent electroactivities into a single engineered hierarchical architecture can substantially enhance the electrochemical properties.[155] Soon afterwards, Kong and co-authors[167] refined this structure and an ultrahigh capacitance of 1693.2 F g^{-1} and an excellent long-term electrochemical stability with only 10.2% capacitance loss after 5000 cycles were obtained (Fig. 12b). Based on these results, Huang *et al.*[68] prepared a similar Co_3O_4 nanowire@MnO_2 (birnessite) composite by a two-step hydrothermal method, which also exhibited high capacitance (560 F g^{-1}) and excellent cycling stability (95% retention after 5000 cycles) (Fig. 12c). In these kinds of nanostructures, the bulk birnessite is replaced by metal oxides which not only ensures that the remaining birnessite can be fully used for energy storage, but also provides a transfer route for charges as the conductivity of Mn-based materials (1×10^{-6} S m^{-1}) is pretty low compared to that of most metal oxides (1×10^{-5}–1×10^{-4} S m^{-1}). However, the applied electrolyte is a big problem for these structures and many electrolytes, including 1.0 M Na_2SO_4, 1.0 M LiOH and 6.0 M KOH, have been tested. However, it is very hard to choose an optimal electrolyte for these two components. For 1.0 M Na_2SO_4 electrolyte, which is very suitable for birnessite, almost no capacitance can be originated for other metal oxides, like NiO, $Ni(OH)_2$, Co_3O_4, $NiCoO_2$, LDH, *etc.* While, if 1.0 M LiOH or 6.0 M KOH was used, the electrochemical performance of birnessite was reduced a lot and these embedded metal oxides also cannot exhibit their full capacitance because of inadequate contact with the electrolyte as they were covered with birnessite. As a consequence, the capacitance calculated for these composites is always lower than that of the embedded metal oxide, while the capacitances calculated based on the weight of birnessite are very high, which means that the dead mass of birnessite can be reduced efficiently by introducing embedded metal oxides.

To well present the uniqueness and difference of these strategies to adjust the electrochemical performance of birnessite based electrodes, their generated electrochemical properties are summarized systematically in Table 1. Generally speaking, the current results are far away from practical requirements.

6. Future prospects

In summary, birnessite based structures are still one of the most promising materials for supercapacitors, and a recent trend in research is to develop birnessites with high conductivity, abundant electrochemically active sites and high utilization rate to reduce the gathering charges, enhance electrochemical reaction sites and reduce dead mass. Benefitting from these integrated advantages, with excellent pseudocapacitive properties, super-high theoretical capacitance and a large voltage window, the supercapacitors fabricated from birnessite are highly desired in energy storage systems with high energy/power density. However, there is still a big gap between the obtained properties and that of available practical electrodes. To overcome this gap, although scientific researchers focus on the regulation of the specific surface area, morphology and conductivity, there are still lots of possibilities in crystalline control, affinity of the electrolyte, special element doping and pore formation to enhance their electrochemical properties. Thus, several possible strategies to further enhance the high electrochemical performance of birnessite based structures for supercapacitor electrodes are listed below:

(i) Increasing the intrinsic electronic conductivity of birnessite. As we discussed above, the electronic conductivity of birnessite is one of the most important points for enhancing its capacitance and rate capability. Introducing heteroatoms, controlling components, and creating defects are some strategies. Although some relative studies have been reported, more studies should be performed, as most of the introduced heteroatoms are common element atoms. Based on this, one possible strategy should be introducing new heteroatoms, for example, rare earth atoms to replace Mn atoms or non-metal atoms to replace O atoms in the crystal lattices of birnessite. Of course, one should not introducing heteroatoms blindly. Design and first principles calculations should be carried out beforehand (Fig. 13a).

(ii) Constructing more smart structures to enhance the utilization of birnessite and its electronic conductivity. Previous reports have demonstrated that building a single or few layer birnessite structure is the most effective approach to enhance the utilization of birnessite as an electrode.[168] However, the electronic conductivity of the prepared structure should be also considered. Constructing single layer birnessite with other 2D conductive materials, like graphene and MXenes, forming a layer-by-layer and sandwich structure should be one of the most optimal strategies, as shown in Fig. 14a and b.[169,170] Additionally, the specific surface area of this constructed structure is boosted maximally. Thus, desirable electrochemical properties, including high specific capacitance, excellent rate capability and long cycling stability are considered a realizable goal. Note that although the electronic conductivity has been enhanced, these constructed structures may not lead to a very desirable ionic conductivity as the pore structure is not well designed. Thus, some follow-up work should be taken into consideration beforehand, like pore formation, incision and spatial arrangement (Fig. 13b).

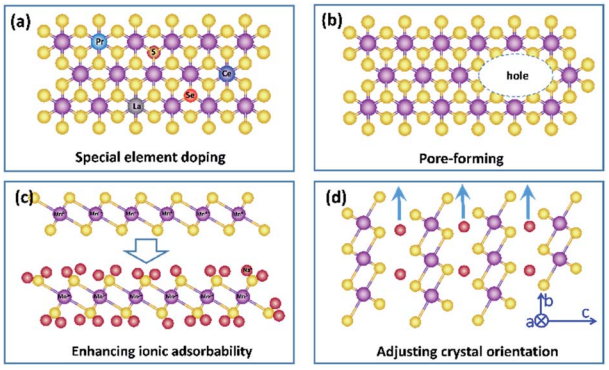

Fig. 13 Possible strategies for developing high performance birnessite based electrodes.

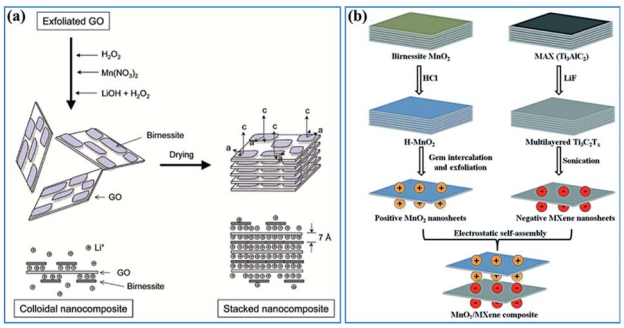

Fig. 14 (a) Schematic representation of GO–birnessite nanocomposites.[169] (b) Illustration of the process of preparing the birnessite/MXene composite.[170]

(iii) Enhancing the electrolyte ionic adsorbability of birnessite. Based on the energy storage mechanism of birnessite, the electrolyte ionic adsorbabilities of birnessite depend on its surface oxygen atoms. Enhancing the adsorption affinity of these oxygen atoms should be a feasible means to boost its specific capacitance. Introducing other nonmetal heteroatoms, altering the interlayer ionic species and adjusting the content of Mn^{4+} are some possible strategies. Particularly, a desirable birnessite single-layer slab composed of Mn^{4+} and all the MnO_6 octahedra can be involved in electrochemical reactions, which will exhibit its theoretical capacitance (Fig. 13c).

(iv) As mentioned in the energy storage mechanism, reducing the dead mass of birnessite by adjusting the crystal orientation of birnessite can be another solution to enhance its electrochemical properties. Increasing the extent of the *c* axis and shortening the extent of the *c* axis and *b* axis will decrease the diffusion-controlled contribution and increase surface capacitive contribution extremely, resulting in an enhanced electrochemical performance (Fig. 13d).

In conclusion, birnessite, as a layered structure of MnO_2, plays an important role in energy storage applications and energy conversion systems because of its low cost, nontoxicity and high operability. To date, birnessite based smart structures with different functions have been extensively investigated and some special architectures also can be applied as energy storage electrodes. We hope that this review can helps us construct more and more smart birnessite based structures for supercapacitors.

Conflicts of interest

There are no conflicts to declare.

Acknowledgements

This work received financial support from the National Natural Science Foundation of China (Grant no. 21576034, 51908092), the Joint Funds of the National Natural Science Foundation of China-Guangdong (Grant no. U1801254), a project funded by the Chongqing Special Postdoctoral Science Foundation (XmT2018043), the Technological projects of Chongqing Municipal Education Commission (KJZDK201800801), and the Innovative Research Team of Chongqing (CXTDG201602014).

References

1 R. McKenzie, *Mineral. Mag.*, 1971, **38**, 493–502.
2 V. A. Drits, E. Silvester, A. I. Gorshkov and A. Manceau, *Am. Mineral.*, 1997, **82**, 946–961.
3 L. Jones and A. A. Milne, *Mineral. Mag. J. Mineral. Soc.*, 1956, **31**, 283–288.
4 E. Silvester, A. Manceau and V. A. Drits, *Am. Mineral.*, 1997, **82**, 962–978.
5 J. E. Post and D. R. Veblen, *Am. Mineral.*, 1990, **75**, 477–489.
6 B. Lanson, V. A. Drits, A. C. Gaillot, E. Silvester, A. Plançon and A. Manceau, *Am. Mineral.*, 2002, **87**, 1631–1645.
7 S. Zhang, K. J. Livi, A. C. Gaillot, A. T. Stone and D. R. Veblen, *Am. Mineral.*, 2010, **95**, 1741–1746.
8 C. Julien, M. Massot, R. Baddour-Hadjean, S. Franger, S. Bach and J. Pereira-Ramos, *Solid State Ionics*, 2003, **159**, 345–356.
9 D. Golden, J. Dixon and C. Chen, *Clays Clay Miner.*, 1986, **34**, 511–520.
10 Q. Feng, K. Yanagisawa and N. Yamasaki, *J. Mater. Sci. Lett.*, 1997, **16**, 110–112.
11 L. Athouël, F. Moser, R. Dugas, O. Crosnier, D. Bélanger and T. Brousse, *J. Phys. Chem. C*, 2008, **112**, 7270–7277.
12 S. Komaba, A. Ogata and T. Tsuchikawa, *Electrochem. Commun.*, 2008, **10**, 1435–1437.
13 H. Jiang, C. Li, T. Sun and J. Ma, *Nanoscale*, 2012, **4**, 807–812.
14 W. Wei, X. Cui, W. Chen and D. G. Ivey, *Chem. Soc. Rev.*, 2011, **40**, 1697–1721.
15 Y. X. Zhang, S. Zhu, M. Dong, C. P. Liu and Z. Q. Wen, *Int. J. Electrochem. Sci.*, 2013, **8**, 2407–2416.
16 Z. Zhang, C. Ma, M. Huang, F. Li, S. Zhu, C. Hua, L. Yu, H. Zheng, X. Hu and Y. Zhang, *J. Mater. Sci.: Mater. Electron.*, 2015, **26**, 4212–4220.
17 X. Fu, X. Wang, Y. Chen, W. Huo, X. Liu, K. Chen, F. Dong, H. C. Yao and Y. Zhang, *J. Colloid Interface Sci.*, 2019, **557**, 168–173.
18 M. Toupin, T. Brousse and D. Bélanger, *Chem. Mater.*, 2004, **16**, 3184–3190.
19 X. Tao, J. Du, Y. Sun, S. Zhou, Y. Xia, H. Huang, Y. Gan, W. Zhang and X. Li, *Adv. Funct. Mater.*, 2013, **23**, 4745–4751.
20 D. Chen, D. Ding, X. Li, G. H. Waller, X. Xiong, M. A. El-Sayed and M. Liu, *Chem. Mater.*, 2015, **27**, 6608–6619.
21 H. Kanoh, W. Tang, Y. Makita and K. Ooi, *Langmuir*, 1997, **13**, 6845–6849.
22 M. Kim and J. Kim, *ACS Appl. Mater. Interfaces*, 2014, **6**, 9036–9045.
23 T. Brousse, M. Toupin, R. Dugas, L. Athouël, O. Crosnier and D. Bélanger, *J. Electrochem. Soc.*, 2006, **153**, A2171–A2180.
24 K. Makgopa, P. M. Ejikeme, C. J. Jafta, K. Raju, M. Zeiger, V. Presser and K. I. Ozoemena, *J. Mater. Chem. A*, 2015, **3**, 3480–3490.

25 Y. Zhang, S. Zhu, X. Hao, C. Liu and Z. Wen, *Ceram. Int.*, 2014, **40**, 13381–13388.
26 C. Liu, Y. Chen, Z. Dong, X. Wu, Y. Situ and H. Huang, *Electrochim. Acta*, 2019, **298**, 678–684.
27 T. Wang, F. Dong and Y. X. Zhang, *Mater. Lett.*, 2016, **171**, 319–322.
28 P. Liu, Y. Zhu, X. Gao, Y. Huang, Y. Wang, S. Qin and Y. Zhang, *Chem. Eng. J.*, 2018, **350**, 79–88.
29 J.-G. Wang, Y. Yang, Z.-H. Huang and F. Kang, *Carbon*, 2013, **61**, 190–199.
30 Z. Q. Wen, M. Li, S. J. Zhu and T. Wang, *Int. J. Electrochem. Sci.*, 2016, **11**, 1810–1820.
31 W. Li, K. Xu, B. Li, J. Sun, F. Jiang, Z. Yu, R. Zou, Z. Chen and J. Hu, *ChemElectroChem*, 2014, **1**, 1003–1008.
32 V. Subramanian, H. Zhu, R. Vajtai, P. Ajayan and B. Wei, *J. Phys. Chem. B*, 2005, **109**, 20207–20214.
33 M. Huang, Y. Zhang, F. Li, L. Zhang, R. S. Ruoff, Z. Wen and Q. Liu, *Sci. Rep.*, 2014, **4**, 3878.
34 J. Chang, M. Jin, F. Yao, T. H. Kim, V. T. Le, H. Yue, F. Gunes, B. Li, A. Ghosh and S. Xie, *Adv. Funct. Mater.*, 2013, **23**, 5074–5083.
35 S. He and W. Chen, *J. Power Sources*, 2015, **294**, 150–158.
36 Z. Fan, J. Yan, T. Wei, L. Zhi, G. Ning, T. Li and F. Wei, *Adv. Funct. Mater.*, 2011, **21**, 2366–2375.
37 L. Yuan, X.-H. Lu, X. Xiao, T. Zhai, J. Dai, F. Zhang, B. Hu, X. Wang, L. Gong and J. Chen, *ACS Nano*, 2011, **6**, 656–661.
38 X. L. Guo, M. Kuang, F. Li, X. Y. Liu, Y. X. Zhang, F. Dong and D. Losic, *Electrochim. Acta*, 2016, **190**, 159–167.
39 G. Liu, C. Kang, J. Fang, L. Fu, H. Zhou and Q. Liu, *J. Power Sources*, 2019, **431**, 48–54.
40 H. Du, C. Wang and J. Lv, *Solid State Commun.*, 2018, **277**, 19–24.
41 J. Lv, M. Yang, T. Liang and H. Miura, *Mater. Lett.*, 2017, **197**, 127–130.
42 L. Yu, G. Q. Zhang, C. Z. Yuan and X. W. Lou, *Chem. Commun.*, 2013, **49**, 137–139.
43 Z. Yu, B. Duong, D. Abbitt and J. Thomas, *Adv. Mater.*, 2013, **25**, 3302–3306.
44 I. I. Misnon and R. Jose, *New J. Chem.*, 2017, **41**, 6574–6584.
45 S.-B. Yoon and K.-B. Kim, *Electrochim. Acta*, 2013, **106**, 135–142.
46 H. Jiang, J. Ma and C. Li, *J. Mater. Chem.*, 2012, **22**, 16939–16942.
47 J. Kang, A. Hirata, L. Kang, X. Zhang, Y. Hou, L. Chen, C. Li, T. Fujita, K. Akagi and M. Chen, *Angew. Chem., Int. Ed.*, 2013, **52**, 1664–1667.
48 L. Liu, M. Min, F. Liu, H. Yin, Y. Zhang and G. Qiu, *J. Power Sources*, 2015, **277**, 26–35.
49 S. Zhu, L. Li, J. Liu, H. Wang, T. Wang, Y. Zhang, L. Zhang, R. S. Ruoff and F. Dong, *ACS Nano*, 2018, **12**, 1033–1042.
50 N. Jabeen, A. Hussain, Q. Xia, S. Sun, J. Zhu and H. Xia, *Adv. Mater.*, 2017, **29**, 1700804.
51 T. Xiong, T. L. Tan, L. Lu, W. S. V. Lee and J. Xue, *Adv. Energy Mater.*, 2018, **8**, 1702630.
52 Y. Liu, D. Yan, Y. Li, Z. Wu, R. Zhuo, S. Li, J. Feng, J. Wang, P. Yan and Z. Geng, *Electrochim. Acta*, 2014, **117**, 528–533.
53 L.-F. Chen, Z.-H. Huang, H.-W. Liang, Q. F. Guan and S. H. Yu, *Adv. Mater.*, 2013, **25**, 4746–4752.
54 X. Lu, M. Yu, G. Wang, T. Zhai, S. Xie, Y. Ling, Y. Tong and Y. Li, *Adv. Mater.*, 2013, **25**, 267–272.
55 Q. Li, Z.-L. Wang, G.-R. Li, R. Guo, L. X. Ding and Y. X. Tong, *Nano Lett.*, 2012, **12**, 3803–3807.
56 L. Bao, J. Zang and X. Li, *Nano Lett.*, 2011, **11**, 1215–1220.
57 P. Yang, Y. Ding, Z. Lin, Z. Chen, Y. Li, P. Qiang, M. Ebrahimi, W. Mai, C. P. Wong and Z. L. Wang, *Nano Lett.*, 2014, **14**, 731–736.
58 Y. He, W. Chen, X. Li, Z. Zhang, J. Fu, C. Zhao and E. Xie, *ACS Nano*, 2013, **7**, 174–182.
59 J. Ge, H.-B. Yao, W. Hu, X. F. Yu, Y. X. Yan, L. B. Mao, H.-H. Li, S.-S. Li and S.-H. Yu, *Nano Energy*, 2013, **2**, 505–513.
60 Z. Zhang, F. Xiao, L. Qian, J. Xiao, S. Wang and Y. Liu, *Adv. Energy Mater.*, 2014, **4**, 1400064.
61 G. Yu, L. Hu, N. Liu, H. Wang, M. Vosgueritchian, Y. Yang, Y. Cui and Z. Bao, *Nano Lett.*, 2011, **11**, 4438–4442.
62 S. Ching, D. J. Petrovay, M. L. Jorgensen and S. L. Suib, *Inorg. Chem.*, 1997, **36**, 883–890.
63 B. M. Tebo, J. R. Bargar, B. G. Clement, G. J. Dick, K. J. Murray, D. Parker, R. Verity and S. M. Webb, *Annu. Rev. Earth Planet. Sci.*, 2004, **32**, 287–328.
64 Q. Feng, H. Kanoh and K. Ooi, *J. Mater. Chem.*, 1999, **9**, 319–333.
65 X. Zhang, P. Yu, H. Zhang, D. Zhang, X. Sun and Y. Ma, *Electrochim. Acta*, 2013, **89**, 523–529.
66 W. Xiao, D. L. Wang and X. W. Lou, *J. Phys. Chem. C*, 2010, **114**, 1694–1700.
67 S. Zhu, W. Cen, L. Hao, J. Ma, L. Yu, H. Zheng and Y. Zhang, *Mater. Lett.*, 2014, **135**, 11–14.
68 M. Huang, R. Mi, H. Liu, F. Li, X. L. Zhao, W. Zhang, S. X. He and Y. X. Zhang, *J. Power Sources*, 2014, **269**, 760–767.
69 Z. Hu, X. Xiao, C. Chen, T. Li, L. Huang, C. Zhang, J. Su, L. Miao, J. Jiang, Y. Zhang and J. Zhou, *Nano Energy*, 2015, **11**, 226–234.
70 G. Wang, L. Zhang and J. Zhang, *Chem. Soc. Rev.*, 2012, **41**, 797–828.
71 S. Zhu, T. Wang, X. Liu, Y. Zhang, F. Li, F. Dong, H. Zhang and L. Zhang, *ACS Appl. Energy Mater.*, 2018, **2**, 1051–1059.
72 J. Liu, C. Xu, Z. Chen, S. Ni and Z. X. Shen, *Green Energy & Environment*, 2018, **3**, 20–41.
73 L. L. Zhang and X. S. Zhao, *Chem. Soc. Rev.*, 2009, **38**, 2520–2531.
74 T. Brousse, D. Belanger and J. W. Long, *J. Electrochem. Soc.*, 2015, **162**, A5185–A5189.
75 W. Gu, M. Sevilla, A. Magasinski, A. B. Fuertes and G. Yushin, *Energy Environ. Sci.*, 2013, **6**, 2465–2476.
76 H. Jiang, P. S. Lee and C. Li, *Energy Environ. Sci.*, 2013, **6**, 41–53.
77 Y. Zhang and D. Xue, *Energy Environ. Focus*, 2012, **1**, 4–18.
78 R. Tholkappiyan, A. N. Naveen, K. Vishista and F. Hamed, *J. Taibah Univ. Sci.*, 2018, **12**, 669–677.
79 T. Qin, S. Dang, J. Hao, Z. Wang, H. Li, Y. Wen, S. Lu, D. He, G. Cao and S. Peng, *Dalton Trans.*, 2018, **47**, 11503–11511.

80 X. Liao, Y. Zhao, J. Wang, W. Yang, L. Xu, X. Tian, Y. Shuang, K. A. Owusu, M. Yan and L. Mai, *Nano Res.*, 2018, **11**, 2083–2092.
81 Z. Sun, Y. Zhang, Y. Liu, J. Fu, S. Cheng, P. Cui and E. Xie, *J. Power Sources*, 2019, **436**, 226795.
82 X. Zhang, Q. Fu, H. Huang, L. Wei and X. Guo, *Small*, 2019, **15**, 1805235.
83 M. Yao, X. Ji, T.-F. Chou, S. Cheng, L. Yang, P. Wu, H. Luo, Y. Zhu, L. Tang, J. Wang and M. Liu, *ACS Appl. Energy Mater.*, 2019, **2**, 2743–2750.
84 Z. Ma, F. Jing, Y. Fan, L. Hou, L. Su, L. Fan and G. Shao, *Small*, 2019, **15**, 1900862.
85 T. C. Liu, W. G. Pell, B. E. Conway and S. L. Roberson, *J. Electrochem. Soc.*, 1998, **145**, 1882–1888.
86 J. Wang, J. Polleux, J. Lim and B. Dunn, *J. Phys. Chem. C*, 2007, **111**, 14925–14931.
87 X. Guo, T. Wang, T. X. Zheng, C. Xu, J. Zhang, Y. X. Zhang, X. Y. Liu and F. Dong, *J. Mater. Chem. A*, 2018, **6**, 24717–24727.
88 M. Sathiya, A. S. Prakash, K. Ramesha, J. M. Tarascon and A. K. Shukla, *J. Am. Chem. Soc.*, 2011, **133**, 16291–16299.
89 N. Jabeen, Q. Xia, S. V. Savilov, S. M. Aldoshin, Y. Yu and H. Xia, *ACS Appl. Mater. Interfaces*, 2016, **8**, 33732–33740.
90 W. Guo, C. Yu, S. Li, Z. Wang, J. Yu, H. Huang and J. Qiu, *Nano Energy*, 2019, **57**, 459–472.
91 J. Hao, Y. Zhong, Y. Liao, D. Shu, Z. Kang, X. Zou, C. He and S. Guo, *Electrochim. Acta*, 2015, **167**, 412–420.
92 C. Xiong, T. Li, M. Khan, H. Li and T. Zhao, *RSC Adv.*, 2015, **5**, 85613–85619.
93 Y. Liu, X. Miao, J. Fang, X. Zhang, S. Chen, W. Li, W. Feng, Y. Chen, W. Wang and Y. Zhang, *ACS Appl. Mater. Interfaces*, 2016, **8**, 5251–5260.
94 Y. Liu, X. Cai, B. Luo, M. Yan, J. Jiang and W. Shi, *Carbon*, 2016, **107**, 426–432.
95 Y. Song, Z. Li, K. Guo and T. Shao, *Nanoscale*, 2016, **8**, 15671–15680.
96 F. Ochai-Ejeh, M. J. Madito, K. Makgopa, M. N. Rantho, O. Olaniyan and N. Manyala, *Electrochim. Acta*, 2018, **289**, 363–375.
97 K. Zhang, H. Zhao, Z. Zhang, J. Chen, X. Mu, X. Pan, Z. Zhang, J. Zhou, J. Li and E. Xie, *Carbon*, 2015, **95**, 746–755.
98 G. Huang, Y. Zhang, L. Wang, P. Sheng and H. Peng, *Carbon*, 2017, **125**, 595–604.
99 M. Hu, C. Cui, C. Shi, Z.-S. Wu, J. Yang, R. Cheng, T. Guang, H. Wang, H. Lu and X. Wang, *ACS Nano*, 2019, **13**, 6899–6905.
100 J. Zhou, H. Zhao, X. Mu, J. Chen, P. Zhang, Y. Wang, Y. He, Z. Zhang, X. Pan and E. Xie, *Nanoscale*, 2015, **7**, 14697–14706.
101 D. Gueon and J. H. Moon, *ACS Sustainable Chem. Eng.*, 2017, **5**, 2445–2453.
102 M. Kim, Y. Hwang, K. Min and J. Kim, *Electrochim. Acta*, 2013, **113**, 322–331.
103 M. Nakayama, S. Osae, K. Kaneshige, K. Komine and H. Abe, *J. Electrochem. Soc.*, 2016, **163**, A2340–A2348.
104 T. Liu, Z. Zhou, Y. Guo, D. Guo and G. Liu, *Nat. Commun.*, 2019, **10**, 675.
105 M. D. Stoller, S. Park, Y. Zhu, J. An and R. S. Ruoff, *Nano Lett.*, 2008, **8**, 3498–3502.
106 L. Peng, X. Peng, B. Liu, C. Wu, Y. Xie and G. Yu, *Nano Lett.*, 2013, **13**, 2151–2157.
107 P. Wu, S. Cheng, L. Yang, Z. Lin, X. Gui, X. Ou, J. Zhou, M. Yao, M. Wang, Y. Zhu and M. Liu, *ACS Appl. Mater. Interfaces*, 2016, **8**, 23721–23728.
108 T. Qiu, B. Luo, M. Giersig, E. M. Akinoglu, L. Hao, X. Wang, L. Shi, M. Jin and L. Zhi, *Small*, 2014, **10**, 4136–4141.
109 S. Zhu, Q. Shan, F. Dong, Y. Zhang and L. Zhang, *Gold Bull.*, 2017, **50**, 61–68.
110 X. Peng, Y. Guo, Q. Yin, J. Wu, J. Zhao, C. Wang, S. Tao, W. Chu, C. Wu and Y. Xie, *J. Am. Chem. Soc.*, 2017, **139**, 5242–5248.
111 C. Zener, *Phys. Rev.*, 1951, **82**, 403–405.
112 G. Wang, Z. Ma, G. Zhang, C. Li and G. Shao, *Electrochim. Acta*, 2015, **182**, 1070–1077.
113 G. Wang, G. Shao, J. Du, Y. Zhang and Z. Ma, *Mater. Chem. Phys.*, 2013, **138**, 108–113.
114 H. Liu, W. Gu, B. Luo, P. Fan, L. Liao, E. Tian, Y. Niu, J. Fu, Z. Wang, Y. Wu, G. Lv and L. Mei, *Electrochim. Acta*, 2018, **291**, 31–40.
115 H. Peng, H. Fan, M. Zhang and L. Ning, *Appl. Phys. A: Mater. Sci. Process.*, 2018, **124**, 482.
116 Q. Peng, L. Liu, Y. Luo, Y. Zhang, W. Tan, F. Liu, S. L. Suib and G. Qiu, *ACS Appl. Mater. Interfaces*, 2016, **8**, 34405–34413.
117 R. Dong, Q. Ye, L. Kuang, X. Lu, Y. Zhang, X. Zhang, G. Tan, Y. Wen and F. Wang, *ACS Appl. Mater. Interfaces*, 2013, **5**, 9508–9516.
118 X. Su, L. Yu, G. Cheng, H. Zhang, M. Sun, L. Zhang and J. Zhang, *Appl. Energy*, 2014, **134**, 439–445.
119 H. Z. Chi, Y. Li, Y. Xin and H. Qin, *Chem. Commun.*, 2014, **50**, 13349–13352.
120 S. Zhao, T. Liu, D. Hou, W. Zeng, B. Miao, S. Hussain, X. Peng and M. S. Javed, *Appl. Surf. Sci.*, 2015, **356**, 259–265.
121 B. Ming, J. Li, F. Kang, G. Pang, Y. Zhang, L. Chen, J. Xu and X. Wang, *J. Power Sources*, 2012, **198**, 428–431.
122 D. Yan, H. Zhang, S. Li, G. Zhu, Z. Wang, H. Xu and A. Yu, *J. Alloys Compd.*, 2014, **607**, 245–250.
123 A. Boisset, L. Athouel, J. Jacquemin, P. Porion, T. Brousse and M. Anouti, *J. Phys. Chem. C*, 2013, **117**, 7408–7422.
124 Z. Li, J. Wang, Z. Wang, H. Ran, Y. Li, X. Han and S. Yang, *New J. Chem.*, 2012, **36**, 1490–1495.
125 S. J. Zhu, J. Zhang, J. J. Ma, Y. X. Zhang and K. X. Yao, *J. Power Sources*, 2015, **278**, 555–561.
126 F. Li, Y. X. Zhang, M. Huang, Y. Xing and L. L. Zhang, *Electrochim. Acta*, 2015, **154**, 329–337.
127 M. Shen, S. J. Zhu, X. Liu, X. Fu, W. C. Huo, X. L. Liu, Y. X. Chen, Q. Y. Shan, H.-C. Yao and Y. X. Zhang, *CrystEngComm*, 2019, **21**, 5322–5331.
128 H. Z. Chi, S. Yin, H. Qin and K. Su, *Mater. Lett.*, 2016, **162**, 131–134.
129 C. Chai, A. Liu, Y. Wang, Y. Lu and H. Che, *Ceram. Int.*, 2018, **44**, 16923–16930.

130 W. Xiao, W. Zhou, H. Yu, Y. Pu, Y. Zhang and C. Hu, *Electrochim. Acta*, 2018, **264**, 1–11.
131 L. Gao, L. Zhang, S. Jia, X. Liu, Y. Wang and S. Xing, *Electrochim. Acta*, 2016, **203**, 59–65.
132 Y. Zhang, M. Dong, S. Zhu, C. Liu and Z. Wen, *Mater. Res. Bull.*, 2014, **49**, 448–453.
133 Y. Munaiah, B. G. S. Raj, T. P. Kumar and P. Ragupathy, *J. Mater. Chem. A*, 2013, **1**, 4300–4306.
134 Z. Q. Wen, M. Li, F. Li, S. J. Zhu, X. Y. Liu, Y. X. Zhang, T. Kumeria, D. Losic, Y. Gao, W. Zhang and S. X. He, *Dalton Trans.*, 2016, **45**, 936–942.
135 Q. J. Le, T. Wang, D. N. H. Tran, F. Dong, Y. X. Zhang and D. Losic, *J. Mater. Chem. A*, 2017, **5**, 10856–10865.
136 Y. Zhang, W. W. Guo, T. X. Zheng, Y. X. Zhang and X. Fan, *Appl. Surf. Sci.*, 2018, **427**, 1158–1165.
137 A. L. M. Reddy, M. M. Shaijumon, S. R. Gowda and P. M. Ajayan, *J. Phys. Chem. C*, 2010, **114**, 658–663.
138 B. Patil, S. Ahn, S. Yu, H. Song, Y. Jeong, J. H. Kim and H. Ahn, *Carbon*, 2018, **134**, 366–375.
139 G.-X. Li, P.-X. Hou, J. Luan, J.-C. Li, X. Li, H. Wang, C. Shi, C. Liu and H.-M. Cheng, *Carbon*, 2018, **140**, 634–643.
140 Q. Wang, Y. Ma, X. Liang, D. Zhang and M. Miao, *Chem. Eng. J.*, 2019, **371**, 145–153.
141 F. Cheng, T. Zhang, Y. Zhang, J. Du, X. Han and J. Chen, *Angew. Chem., Int. Ed.*, 2013, **52**, 2474–2477.
142 M. K. Song, S. Cheng, H. Chen, W. Qin, K.-W. Nam, S. Xu, X.-Q. Yang, A. Bongiorno, J. Lee, J. Bai, T. A. Tyson, J. Cho and M. Liu, *Nano Lett.*, 2012, **12**, 3483–3490.
143 T. Zhai, X. Lu, F. Wang, H. Xia and Y. Tong, *Nanoscale Horiz.*, 2016, **1**, 109–124.
144 Y. Huang, Y. Li, Z. Hu, G. Wei, J. Guo and J. Liu, *J. Mater. Chem. A*, 2013, **1**, 9809–9813.
145 P. Gao, P. Metz, T. Hey, Y. Gong, D. Liu, D. D. Edwards, J. Y. Howe, R. Huang and S. T. Misture, *Nat. Commun.*, 2017, **8**, 14559.
146 Y. Wang, Y. Lu, K. Chen, S. Cui, W. Chen and L. Mi, *Electrochim. Acta*, 2018, **283**, 1087–1094.
147 W. He, C. Wang, F. Zhuge, X. Deng, X. Xu and T. Zhai, *Nano Energy*, 2017, **35**, 242–250.
148 G. Nie, X. Lu, M. Chi, Y. Zhu, Z. Yang, N. Song and C. Wang, *Electrochim. Acta*, 2017, **231**, 36–43.
149 Z. Ma, G. Shao, Y. Fan, G. Wang, J. Song and D. Shen, *ACS Appl. Mater. Interfaces*, 2016, **8**, 9050–9058.
150 H. Y. Wang, F. X. Xiao, L. Yu, B. Liu and X. W. Lou, *Small*, 2014, **10**, 3181–3186.
151 Y. Guo, L. Yu, C. Y. Wang, Z. Lin and X. W. Lou, *Adv. Funct. Mater.*, 2015, **25**, 5184–5189.
152 Y. Guo, C. Wu, N.-W. Li, S. Yuan and L. Yu, *J. Mater. Chem. A*, 2019, DOI: 10.1039/c9ta05790k.
153 W. Xiao, J. S. Chen and X. W. Lou, *CrystEngComm*, 2011, **13**, 5685–5687.
154 S. J. Zhu, J. Q. Jia, T. Wang, D. Zhao, J. Yang, F. Dong, Z. G. Shang and Y. X. Zhang, *Chem. Commun.*, 2015, **51**, 14840–14843.
155 J. Liu, J. Jiang, C. Cheng, H. Li, J. Zhang, H. Gong and H. J. Fan, *Adv. Mater.*, 2011, **23**, 2076.
156 M. Huang, Y. Zhang, F. Li, Z. Wang, Alamusi, N. Hu, Z. Wen and Q. Liu, *Sci. Rep.*, 2014, **4**, 4518.
157 J. Liu, J. Jiang, M. Bosman and H. J. Fan, *J. Mater. Chem.*, 2012, **22**, 2419–2426.
158 H. Jiang, C. Li, T. Sun and J. Ma, *Chem. Commun.*, 2012, **48**, 2606–2608.
159 M. U. A. Prathap, V. Anuraj, B. Satpati and R. Srivastava, *J. Hazard. Mater.*, 2013, **262**, 766–774.
160 M. Kundu, G. Singh and A. M. Svensson, *New J. Chem.*, 2019, **43**, 1257–1266.
161 Z. Wang, F. Wang, J. Tu, D. Cao, X. An and Y. Ye, *Mater. Lett.*, 2016, **171**, 10–13.
162 H. Chen, X. L. Liu, J. M. Zhang, F. Dong and Y. X. Zhang, *Ceram. Int.*, 2016, **42**, 8909–8914.
163 R. J. Ramalingam, N. Konikkara, H. Al-Lohedan, D. M. Aldhayan, L. J. Kennedy, S. K. K. Basha and S. R. M. Sayed, *Int. J. Hydrogen Energy*, 2018, **43**, 17121–17131.
164 X. Hao, Y. Zhang, Z. Diao, H. Chen, A. Zhang and Z. Wang, *RSC Adv.*, 2014, **4**, 63901–63908.
165 W. Quan, C. Jiang, S. Wang, Y. Li, Z. Zhang, Z. Tang and F. Favier, *Electrochim. Acta*, 2017, **247**, 1072–1079.
166 W. Zheng, S. Sun, Y. Xu, R. Yu and H. Li, *J. Alloys Compd.*, 2018, **768**, 240–248.
167 D. Kong, J. Luo, Y. Wang, W. Ren, T. Yu, Y. Luo, Y. Yang and C. Cheng, *Adv. Funct. Mater.*, 2014, **24**, 3815–3826.
168 Z. Liu, K. Xu, H. Sun and S. Yin, *Small*, 2015, **11**, 2182–2191.
169 X. J. Yang, Y. Makita, Z. H. Liu and K. Ooi, *Chem. Mater.*, 2003, **15**, 1228–1231.
170 S. Chen, Y. Xiang, W. Xu and C. Peng, *Inorg. Chem. Front.*, 2019, **6**, 199–208.

